



HAL
open science

Seasonal and interannual variability of the Eastern Tropical Pacific Fresh Pool

S. Guimbard, N. Reul, B. Chapron, M. Umbert, C. Maes

► **To cite this version:**

S. Guimbard, N. Reul, B. Chapron, M. Umbert, C. Maes. Seasonal and interannual variability of the Eastern Tropical Pacific Fresh Pool. *Journal of Geophysical Research. Oceans*, 2017, 122, pp.1749-1771. 10.1002/2016JC012130 . insu-03682754

HAL Id: insu-03682754

<https://insu.hal.science/insu-03682754>

Submitted on 1 Jun 2022

HAL is a multi-disciplinary open access archive for the deposit and dissemination of scientific research documents, whether they are published or not. The documents may come from teaching and research institutions in France or abroad, or from public or private research centers.

L'archive ouverte pluridisciplinaire **HAL**, est destinée au dépôt et à la diffusion de documents scientifiques de niveau recherche, publiés ou non, émanant des établissements d'enseignement et de recherche français ou étrangers, des laboratoires publics ou privés.

Copyright

RESEARCH ARTICLE

10.1002/2016JC012130

Seasonal and interannual variability of the Eastern Tropical Pacific Fresh Pool

S. Guimbard¹ , N. Reul¹, B. Chapron¹, M. Umberto¹ , and C. Maes¹ ¹Laboratoire d'Océanographie Physique et Spatiale, Ifremer, CNRS, IRD, IUEM, Univ. Brest, Brest, France

Key Points:

- Satellite SSS in synergy with complementary EO data allows studying the seasonal and interannual dynamics of the Eastern Pacific Fresh Pool
- Fresh pool zonal displacements and links between surface and subsurface processes respond to freshwater fluxes, wind stress, and currents
- Fresh pool interannual variability is related to ENSO phases, a maximal extension was reached in 2015 coinciding with a strong El Niño event

Correspondence to:

S. Guimbard,
sebastien.guimbard@ifremer.fr

Citation:

Guimbard, S., N. Reul, B. Chapron, M. Umberto, and C. Maes (2017), Seasonal and interannual variability of the Eastern Tropical Pacific Fresh Pool, *J. Geophys. Res. Oceans*, 122, 1749–1771, doi:10.1002/2016JC012130.

Received 7 JUL 2016

Accepted 3 FEB 2017

Accepted article online 11 FEB 2017

Published online 4 MAR 2017

Abstract The Eastern Pacific Fresh Pool (EPFP) is a large region of low sea surface salinity (SSS) defined by values lower than 34 practical salinity scale within (5°S–30°N, 75°W–180°W). The fresh pool dynamically responds to strong regional and seasonally varying ocean-atmosphere-land interactions (including monsoon rain, trade and gap winds, and strong currents). Using more than 5 years of Soil Moisture and Ocean Salinity (SMOS) satellite sea surface salinity (SSS) and complementary satellite wind, rain, currents, and sea surface temperature data together with a historical ensemble of in situ products, the present study explores the seasonal and interannual dynamics of the fresh pool over the period 2004–2015. An important interannual variability of the maximal surface extension of the EPFP over the past decade is revealed with two extreme events (2012, 2015) occurring during the SMOS satellite period. These extremes are found to be related to the El Niño–Southern Oscillation (ENSO) phases and associated anomalies of precipitation, surface currents, and trade wind in the central Pacific. In 2012 (La Niña), stronger trade winds coupled with a deficit of precipitation induced a minimum extension of the pool during the rainy season. Whereas, during the strong El Niño 2014–2015, the EPFP extension reached an unprecedented maximum value. A modification of the atmospheric freshwater fluxes and ocean surface currents during winter 2014 is found to have favored the onset of this abnormal fresh event.

1. Introduction

One of the most conspicuous features of the tropical Pacific Ocean surface salinity field (Figure 1) is the presence of a zonal band of low-salinity waters (below 34.5) which extends across the entire basin at latitudes between 2°N and 15°N [Lynn, 1964; Hires and Montgomery, 1972]. The intensity and meridional width of that freshwater band vary across the basin. The band is saltier and narrowest around the dateline. To the east and west of the dateline, it becomes fresher and wider. West of 160°W, surface waters with salinities lower than 34.8 and temperature $T > 28^{\circ}\text{C}$, as observed in the World Ocean Atlas annual climatology (WOA 2013, version 2) are defining the West Pacific fresh pool (WPFP). East of 130°W, the upper ocean salinity drops below 34 with $T > 25^{\circ}\text{C}$, defining the so-called Tropical Surface Water (TSW) [Wyrski, 1966; Wyrski and Kendall, 1967] to form the Eastern Pacific Fresh Pool [Fiedler et al., 1992; Fiedler and Talley, 2006], hereafter denoted EPFP. On the far eastern side of the EPFP (east of 95°W), sea surface salinity (SSS) further decreases below 33 all year long which is the lowest SSS observed in the tropical Pacific [Boyer and Levitus, 2002]. North of the Equator, these low-salinity waters are mainly due to intense and persistent rainfall under the Inter-Tropical Convergence Zone (ITCZ) [Trenberth and Hurrell, 1994; Amador et al., 2006].

Monitoring the large-scale SSS patterns and their zonal interannual evolution is possibly key in the context of El Niño and could lead to better forecasts [Zhu et al., 2014]. As shown by Singh et al. [2011], the so-called “Eastern Pacific” (EP) El Niño events result in large (30° longitude) eastward displacements of the eastern edge of the west Pacific low-salinity warm pool waters and a resulting well-marked SSS freshening (~ 1) near the dateline. During El Niño (respectively, La Niña), sea surface salinity decreases (respectively, increases) in the western and central equatorial Pacific, as a result of zonal advection of low (respectively, high) salinity water by anomalous eastward (respectively, westward) surface currents, and as a result of excess (respectively, deficit) rainfall associated with warm water displacements and enhanced atmospheric convection [Picaut et al., 1996]. Large precipitation anomalies occur from meridional shifts in the location of the intertropical convergence zone (ITCZ), or South Pacific convergence zone (SPCZ), during El Niño events [Trenberth and Caron, 2000]. These shifts are associated with complex large-scale feedback mechanisms

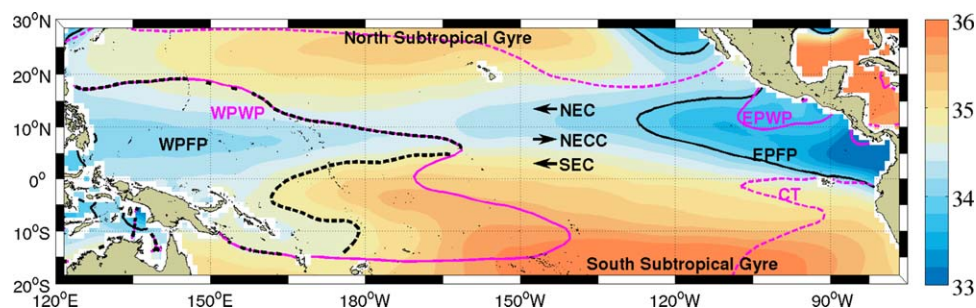


Figure 1. World Ocean Atlas (WOA 2013, version 2) annual climatology at the surface (decadal average 1955–2012) is in shaded color. Curves in black, dashed black, magenta, and dashed magenta define the surface 34-isohaline, the isoline with $SSS = 34.8$ and $SST = 28$, 28 , and 24°C isotherms, respectively. The North Equatorial Current (NEC), the North Equatorial Countercurrent (NECC), and the South Equatorial Current (SEC) are represented by schematic black arrows. Location of the Eastern (EPFP) and Western (WPWP) Pacific fresh pools, Eastern (EPWP) and Western (WPWP) Pacific warm pools, Cold Tongue (CT), and North/South subtropical gyres are also indicated.

between ocean and atmosphere in these conditions [e.g., Bjerknes, 1969; Xie, 1994; Zhang *et al.*, 2009]. Interannual changes in SST induce coherent fluctuations in the atmospheric circulation, including changes in precipitation (P) and evaporation (E), whose interannual variabilities have been well documented in association with ENSO [e.g., Xie and Arkin, 1995; Yu and Weller, 2007].

While many past studies have focused on the impact of El Niño on the WPFP, and the eastward displacement of the SSS front along the equator [Maes *et al.*, 2002, 2005], very little is known about the dynamical response of the TSW and EPFP to ENSO. Recent works [Alory *et al.*, 2012] have analyzed the seasonal dynamics of the freshest surface waters (<33) found in the most eastern part of the EPFP, but still little is known on the seasonal dynamics of the TSW, with intermediate salinities in the range 33–34. As reported by Alory *et al.* [2012], the lowest values of SSS (<33) appear off Panama due to the strong monsoon summer rains and associated river runoff linked with the northward migration of the ITCZ over Central America in June. This 33-isohaline at the ocean surface seasonally migrates eastward from a most western longitude of about 95°W , reached during the first half of the year, to 85°W from June to December (cf. Figure 2, white contours). This is somehow at variance with the 34-isohaline which exhibits a different seasonal variability (Figure 2), expanding continuously westward throughout the year, starting from about 125°W at the beginning of the year to reach about 160°W in the last quarter.

The recent results of Yu [2014, 2015] clearly indicate that SSS in this EPFP region is not only modulated by the E-P forcing but also strongly affected by the wind-driven oceanic circulation. The newly available SSS satellite observations, from the ESA Soil Moisture and Ocean Salinity (SMOS) and NASA/SAC-D Aquarius missions, launched in November 2009 and June 2011, respectively, provide an opportunity to study the EPFP interannual variability during a particularly active period including both a La Niña (2010–2012) and an El Niño (2014–2016) phase. The present paper focuses on the fresh pool zonal displacements, combining SSS fields with a suite of Earth observation (EO) data, namely complementary satellite wind, rain, sea surface temperature, and inferred currents. The goal is to document the interannual variability of the pool salinity and of its major forcing fields. The potential links between the pool surface and subsurface characteristics are further analyzed.

The paper is organized as follows. The data used in the present study are described in section 2. In section 3, the seasonal variability of SSS and its forcing fields is analyzed over 2010–2015. Varying characteristics between the surface and subsurface signatures in salinity are addressed to reveal the tridimensional (3-D) structure of the eastern Pacific fresh pool. In section 4, the interannual variability is analyzed with a focus on two extreme years, namely 2012 and 2015, exhibiting two extrema over the last decade in the pool maximum areal extent. Major physical processes involved in the observed interannual variability of the fresh pool in that region are finally discussed.

2. Data Description

2.1. SMOS Data

For this study, we used the new Ifremer Level 4a SSS thematic research products available from CNES-IFREMER Centre Aval de Traitement des Données SMOS (CATDS) at IFREMER. These products are weekly SMOS SSS composite at half-degree resolution, bias-corrected at large-scale ($10^\circ \times 10^\circ$) using monthly in situ

ISAS objectively analyzed fields [Gaillard *et al.*, 2009]. The products temporal coverage is May 2010 to December 2015. All relevant information about this data set can be found in Reul and Ifremer CATDS-CECOS Team [2015] and Reul *et al.* [2015]. These products also include an ensemble of geophysical parameters (sea surface temperature, wind speed, precipitation and evaporation rate, mixed layer depth, wind stress, surface current components) derived from well-acknowledged products in the scientific communities that are useful for synergistic science applications using SMOS data. These fields are averaged or accumulated in time—or interpolated—over the week of each SMOS L4a SSS product and gridded at the same 1/2° spatial resolution. A matchup database of colocalized (radius of ±25 km) SMOS SSS with in situ upper ocean data available for each week is also provided with the products. Statistics of the comparison between satellite-based 0.5°, weekly products and in situ measurements reveal a root mean square difference of ~0.3 (see Appendix A).

2.2. Other Earth Observation Data

2.2.1. In Situ Observations

1. An ensemble of Argo float upper-level measurements provided by the Coriolis data center is collected during the L4 SSS product period (May 2010 to December 2014). Only delayed mode Argo salinity and

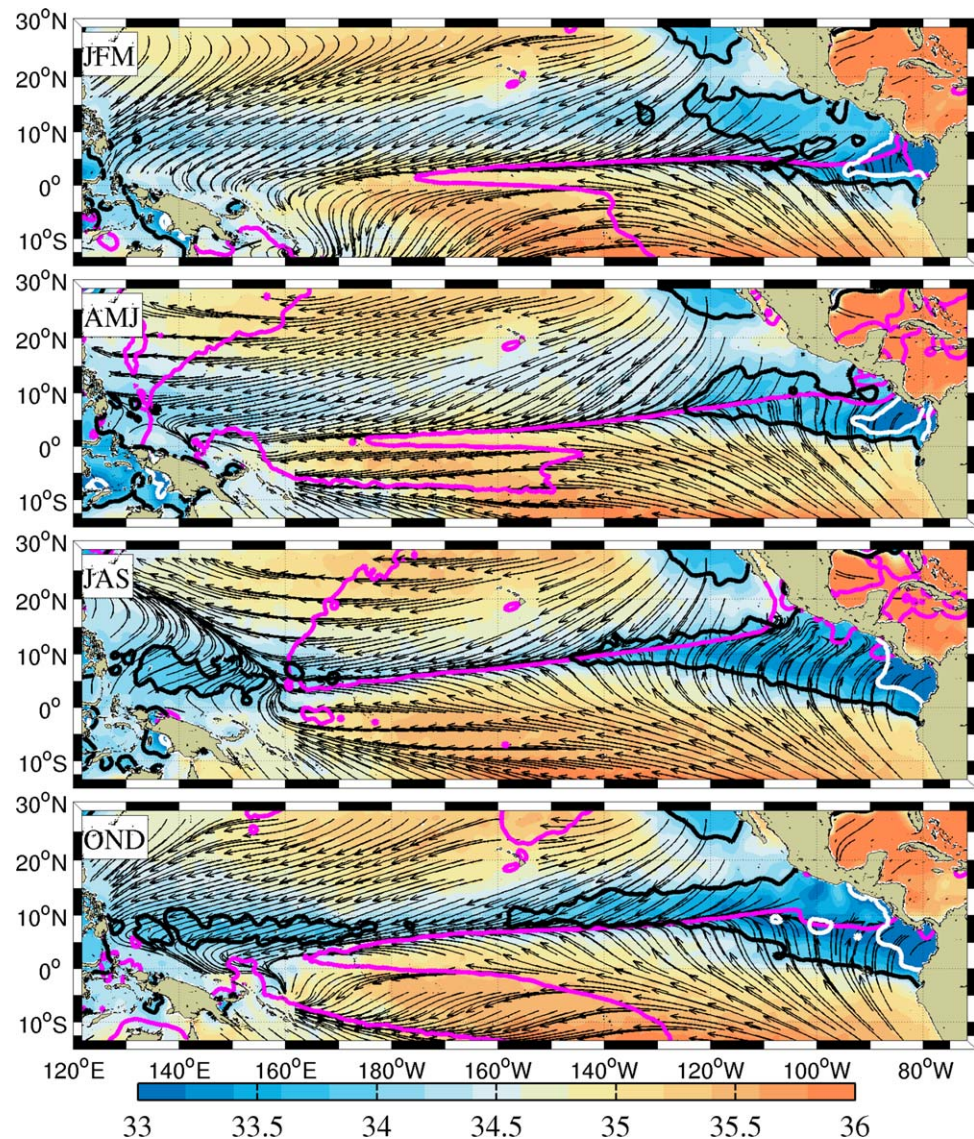


Figure 2. WOA SSS seasonal climatology maps in the Tropical Pacific. The black, white and magenta curves indicate the 34-isohaline, 33-isohaline, and the ITCZ positions, respectively. The black arrows indicate the quarterly mean wind stress from the SCOW. From top to bottom the trimonthly average corresponds to JFM, AMJ, JAS, and OND.

temperature float data with quality index equal 1 and 2 were considered. The upper ocean salinity and temperature values recorded between 0 and 10 m depth are considered as Argo sea surface salinities and will be referred to as Argo SSS and SST.

2. Thermosalinograph (TSG) data from May 2010 to December 2014 are provided by the GOSUD V3 delayed-mode data sets. Adjusted values (if available) with quality flags = 1 or 2 were considered. The data set was complemented by adding thermosalinometer data from the French research vessels [Gaillard *et al.*, 2015]. Note that delayed-mode data are only available until end 2013 at the time of this study. In addition, we considered the “research” quality data from the U.S. Shipboard Automated Meteorological and Oceanographic System (SAMOS) initiative.
3. Surface time series of salinity from the Tropical Atmosphere Ocean (TAO/TRITON) Array were also collected and colocalized with SMOS L4 data. Only data measured at 1 m depth with standard quality (pre-deployment calibration applied) and highest quality (pre/post calibration agree) flags were selected.

2.2.2. Climatology and Objectively Analyzed In Situ S and T Data

1. Monthly climatological fields of SSS from the World Ocean Atlas 2013 (WOA13) V2 [Boyer *et al.*, 2015] decadal average (1955–2012) were used for this study (e.g., Figures 1 and 2).
2. Vertical (every 5 m down to 100 m depth) and horizontal (with $1/2^\circ \times 1/2^\circ$ resolution) optimally interpolated monthly fields of in situ salinity and temperature data generated using the In Situ Analysis System (ISAS) [Gaillard *et al.*, 2016] are used to describe the vertical hydrographic structure of the fresh pool over 2010–2015. This data set corresponds to INSITU_GLO_TS_OA_NRT_OBSERVATIONS_013_002_a which is available via Copernicus Marine environment monitoring service only from January 2010. Historical characteristics of the EFPF from 2004 to 2010, as presented in Figure 8, were determined using ISAS-13 data set [Gaillard, 2015].
3. For the Mixed Layer Depth (MLD) and Top of the Thermocline Depth (TTD) estimates, we used the monthly $1^\circ \times 1^\circ$ MLD product available at the International Pacific Research Center/Asia-Pacific Data-Research Center (IPRC/APDRC). The MLD is defined here as the depth at which density increases from its value at 10 m depth to the value equivalent to a temperature drop of 0.2°C [de Boyer Montégut *et al.*, 2004, 2007] and the TTD is the depth at which temperature decreases from its 10 m value by 0.2°C .

2.2.3. Precipitation

Precipitation is estimated using the CMORPH 3 hourly products at $1/4^\circ$ resolution [Joyce *et al.*, 2004].

2.2.4. Scatterometer Wind Stress

1. Monthly climatology of the surface wind stress components from the Scatterometer Climatology of Ocean Winds (SCOW) [Risien and Chelton, 2008] is used in Figure 2 to draw the historical picture of the seasonal wind stress variability and ITCZ location (i.e., meridional wind stress equal zero), and in Figure 1 to draw the annual position of the ITCZ.
2. Surface wind stress component included into the SMOS L4a products is based on the Advanced Scatterometer (ASCAT) daily data produced and made available at Ifremer/cersat on a $0.25^\circ \times 0.25^\circ$ resolution grid [Bentamy and Fillon, 2012]. The daily $1/4^\circ$ resolution fields were averaged at the SMOS L4 products $1/2^\circ$ resolution and the mean wind stress components over the 7 day period of the SMOS L4a product were evaluated.

2.2.5. Sea Surface Temperature

Sea Surface Temperature (SST) is coming from European Centre for Medium-Range Weather Forecasts (ECMWF) model forecasts, based on analyses received from the Met Office Operational Sea Surface Temperature and Sea Ice Analysis (OSTIA) [Donlon *et al.*, 2012] swath product and was averaged in space and time the same way as the SMOS SSS.

2.2.6. Evaporation

For ocean evaporation, we used the data from the Objectively Analyzed Air-sea Fluxes (OAFflux) project [Yu, 2007], available from the Woods Hole Oceanographic Institution (WHOI), from May 2010 to April 2016. The daily 1° gridded OAFflux evaporation products were spatially interpolated (bilinear) on the SMOS product $1/2^\circ$ grid and accumulated in time over the 7 day period corresponding to the SMOS L4a product.

2.2.7. Surface Currents

1. Near-surface currents derived from satellite-tracked surface drifting buoy observations (Global Drifter Program) are used in Figure 12, including data until December 2015 [Lumpkin and Johnson, 2013].
2. The $1/3^\circ$ resolution global surface current products from Ocean Surface Current Analyses Realtime (OSCAR) [Bonjean and Lagerloef, 2002] were used. They are directly calculated from satellite altimetry and

ocean vector winds. The $1/3^\circ$ resolution 5 day OSCAR data were regridded on a $1/2^\circ$ resolution grid and the 5 day currents fields were linearly interpolated in time on a daily basis. The mean current components provided into the L4a products are then the result of a time averaging over the 7 day period of the SMOS L4a product.

3. East Pacific Fresh Pool Seasonal Variability Over 2010–2015

3.1. Seasonal Variability of SSS and Forcing Fluxes

The seasonal variability of SSS, associated forcing fluxes (E-P, surface currents and wind stress) and upper ocean layer characteristics (such as MLD) as observed over 2010–2015 in the EPFP are successively presented hereafter.

The westernmost front of the fresh pool, defined by $S \leq 34$, is observed in SMOS bimonthly averaged SSS fields (Figure 3) around 120°W from January to April then continuously extends westward throughout the rest of the year to reach $\sim 170^\circ\text{W}$ in October–November.

During December to March, the western border of the pool exhibits a remarkable meridional S-shape associated with an eastward incursion of slightly saltier surface waters ($34 < S < 34.5$) centered around 6°N and extending eastward up to 110°W in February–March. This saltier water tongue separates two distinct branches of the EPFP during that period (1) a northern branch extending meridionally from $\sim 8^\circ\text{N}$ to 16°N , and zonally from 120°W to the central American coasts, and (2) a meridionally thinner southern branch centered around 3°N and extending westward from the Colombia and Ecuador coasts to $\sim 115^\circ\text{W}$. The region of the slightly saltier tongue seems to be progressively filled up by fresher water in April–May to form a meridionally unified fresh pool around May.

During the next following 6 months of the year, the fresh pool western tip continuously extends westward around a central latitude of $\sim 8^\circ\text{N}$, with an average rate of displacement of about 6° of longitude per month, to reach $\sim 170^\circ\text{W}$ at the end of the year. The fresh pool meridional width is decreasing progressively westward from 1000–1500 km east of 110°W to ~ 400 km west of that longitude.

As found previously [e.g., Fiedler and Talley, 2006; Alory et al., 2012; Wang et al., 2013; Yu, 2014, 2015], the Evaporation minus Precipitation (E-P) net flux also exhibits a significant seasonal variation in the EPFP region (Figure 3, right plots).

During the dry winter season (January–April), evaporation dominates precipitation over most of the northern branch of the pool (north of 6°N) while a weakly precipitation-dominated zone is found around and south of the ITCZ.

During the rainy season (May–October), the freshwater flux meridional distribution is reversed and follows the northward migration of the ITCZ. Precipitation thus dominates evaporation north of 3°N – 4°N and (E-P) progressively becomes positive south of this latitude. The most western tip of the low SSS pool coincides with the location of the ITCZ. As discussed in Yu [2014, 2015], the low-salinity pool stops following the southward migration of the ITCZ towards 6°N the last 2 months of the year and stays centered around 8°N .

Equatorial surface currents play an important role in the seasonal variation of SSS (Figure 4). The saltier tongue that is responsible for the S-shape of the western boundaries of the pool in January–February is clearly located within a latitude band (5°N – 7°N) where the North Equatorial Counter Current (NECC) exhibits a strong eastward circulation. Contrarily, the two north and south neighboring branches of the EPFP are areas under the influence of the westward flowing North and South Equatorial currents, respectively.

While the NECC weakens in intensity in March–April, it then reintensifies in May to generate a constant band of eastward flowing circulation east of the dateline within the 5°N – 7°N band. The EPFP westward extension during the second half of the year is mainly detected north of that counter current band.

The seasonal dynamics of the EPFP is also strongly interconnected with the seasonal variability of the wind stress distribution over the basin (Figure 4, right plots). From boreal spring to autumn (May–October), west of 120°W , the fresh pool is extending westward along the calm wind bands centered around the ITCZ. During that period, the trade winds in the North subtropical gyre reach their minimum seasonal intensity and they start to reintensify beginning of the winter season. When the pool is reaching its maximal westward extension in November, the northern flanks of the pool (with respect the ITCZ) within 120°W – 180°W are

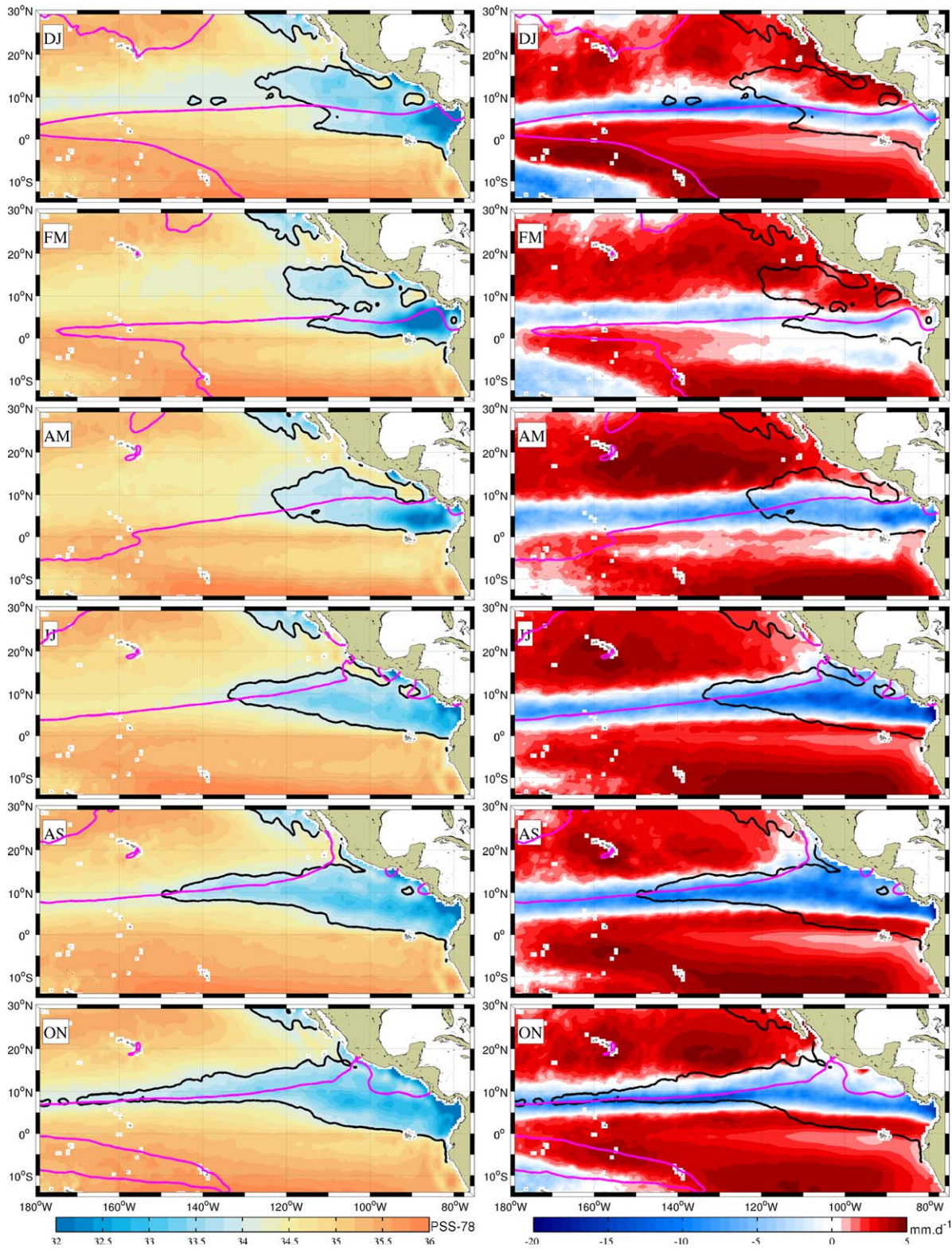


Figure 3. Bimonthly SMOS SSS (left) and Evaporation minus Precipitation in mm/d (right) averaged over 2010–2015. The black and pink thick contours are the 34 isohaline and location of the ITCZ, respectively. From top to bottom the bimonthly average corresponds to months of December–January (DJ); February–March (FM); April–May (AM); June–July (JJ); August–September (AS); October–November (ON).

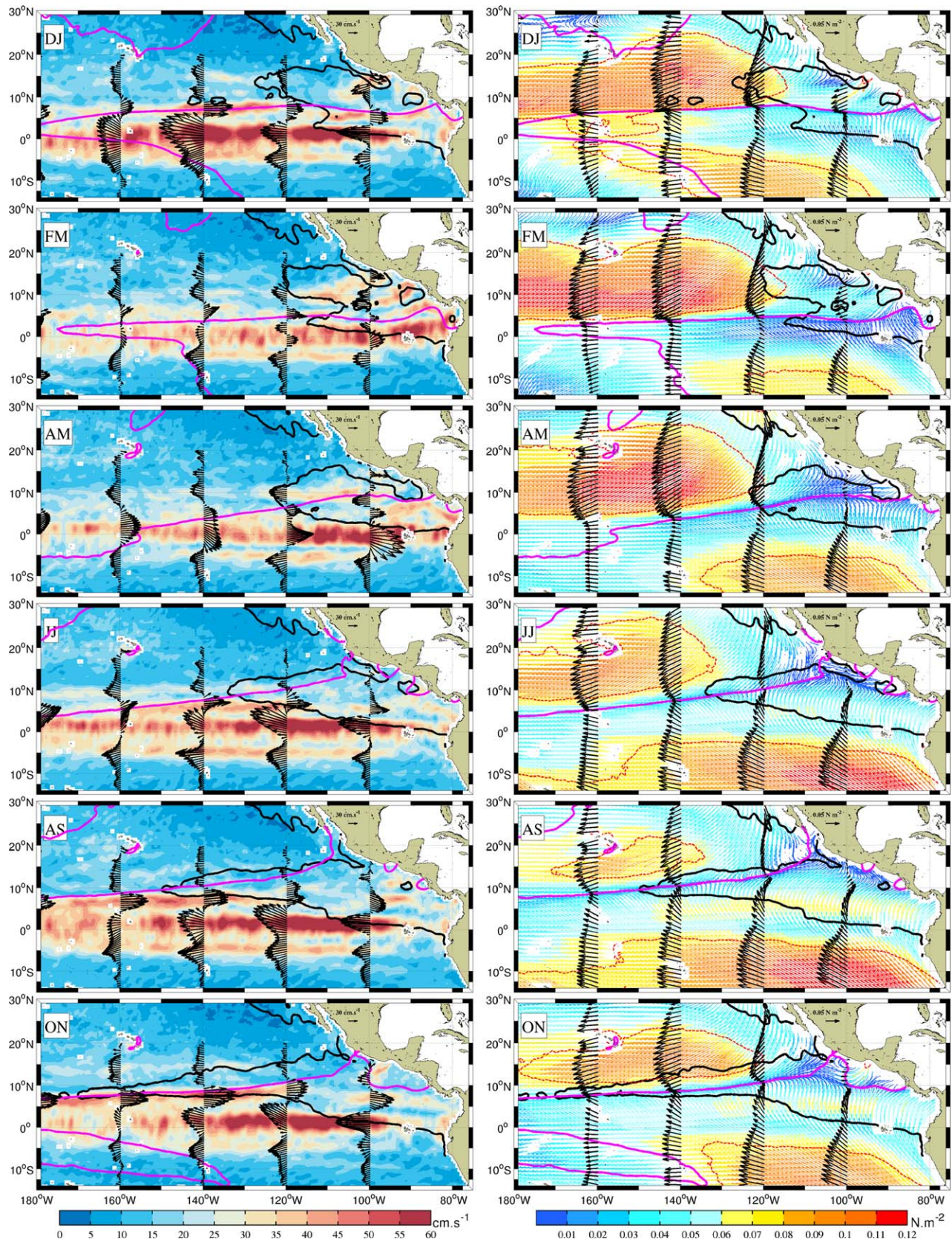


Figure 4.

then subjected to relatively strong south-westward blowing wind stresses ($|\tau| > 0.1 \text{ N m}^{-2} \iff U_{10}^N \sim 7\text{--}8 \text{ m/s}$).

During the minimum zonal extension period of the pool (January–April), the trade winds in the North subtropical gyre reach their maximum intensity ($|\tau| > 0.12 \text{ N m}^{-2}$), and, except for the north-western tip of the pool and the coastal gap wind area, the EPFP mostly stays confined to the east within a calm wind area.

The vertical Ekman pumping velocity distribution (Figure 5, left plots) defined by $w_E = 1/\rho \text{ curl}(\tau/f)$ shows a west-east extended band of $\sim 3\text{--}4^\circ$ of latitude width of upwards velocity ($\sim 0.5 \text{ m/d}$), seasonally migrating within the pool with the wind convergence zone. In January–February, the wind-driven upwelling band exhibits a maximum in w_E intensity and is aligned with the NECC and the saltier tongue separating the northern and southern branches of the pool.

The Mixed Layer Depth (MLD) within the fresh pool is systematically shallower than about 35 m and mostly follows the seasonal wind stress distribution (Figure 5, right plots). The MLD shows minimum values ($< 15 \text{ m}$) in the far eastern region (east of 100°W) subjected to calm winds while deeper MLD ($> 30 \text{ m}$) are found in the north and western parts of the pool which are under the action of higher wind stresses in December–May and October–November, respectively.

3.2. Surface Versus Subsurface Seasonal Extent Variability

To gain insight into the seasonal cycle of the vertical and horizontal extents of the EPFP, we combined monthly SMOS averaged SSS with the in situ objectively analyzed ISAS fields. Composites were built up by simply replacing the upper-level surface ISAS monthly fields by the SMOS ones.

The EPFP appears clearly as a “body of water” (Figure 6), with March–April and October–November corresponding to the minimal and maximal extension periods of the pool, respectively. The EPFP is in general shallower than 60 m but the distribution of its vertical extent is highly variable both in space within the pool itself and as a function of the seasons (Figure 7).

From December to April, the two southern and northern branches of the EPFP are in general deeper ($> 30 \text{ m}$) than its central part, that forms a shallow layer ($< 20 \text{ m}$) extending from the eastern tip of the salty tongue discussed previously (6°N , 100°W) to the Costa-Rica dome. The northern branch of the EPFP is significantly deeper ($> 40 \text{ m}$) than its southern counterpart ($\sim 20\text{--}40 \text{ m}$).

As the pool southern and northern branches unite at the surface in spring, its vertical extent becomes more uniform $\sim 35 \text{ m}$ except for (i) a deeper patch $> 40 \text{ m}$ in the central part of the pool (centered around 10°N , 110°W) and (ii) a shallower patch centered at 9°N , 90°W around the Costa-Rica dome. From boreal summer to beginning of winter, a deeper than 40 m freshwater tongue extends on the southern part of the EPFP from $\sim 120^\circ\text{W}$ to $\sim 90^\circ\text{W}$.

During the second half of the year, as the EPFP extends westward, the surface freshwater lens west of 120°W is significantly shallower ($\sim < 20 \text{ m}$) than east of that longitude. In the central eastern Pacific between 155°W and 180°W , surface SSS measured by SMOS reveal lenses fresher than 34 in October–November. This signal is not similarly detected by in situ ISAS at 5 m depth, potentially indicating a very shallow freshwater cap only detectable by microwave satellite sensors [Boutin *et al.*, 2015].

In order to further quantify the EPFP seasonal variability, the fresh pool surface area and volume are, respectively, computed as

$$S = \iint_A (\Gamma(34 - \text{SSS}(x, y))) dx dy \quad (1)$$

and

Figure 4. Bimonthly OSCAR surface currents in cm s^{-1} (left) and ASCAT wind stresses fields in N m^{-2} (right) averaged over 2010–2015. The black and magenta thick contours are the 34 isohaline and location of the ITCZ, respectively. From top to bottom the bimonthly average corresponds to months as shown in Figure 3. The black arrows enhance the intensity (arrows length) and direction of the surface currents (left column) and the wind stress (right column) at four specific bands of longitudes (180°W , 160°W , 140°W , 120°W). In the right column, the dashed red contours correspond to the locations where $\tau = 0.08 \text{ N m}^{-2} \approx 7 \text{ m s}^{-1}$.

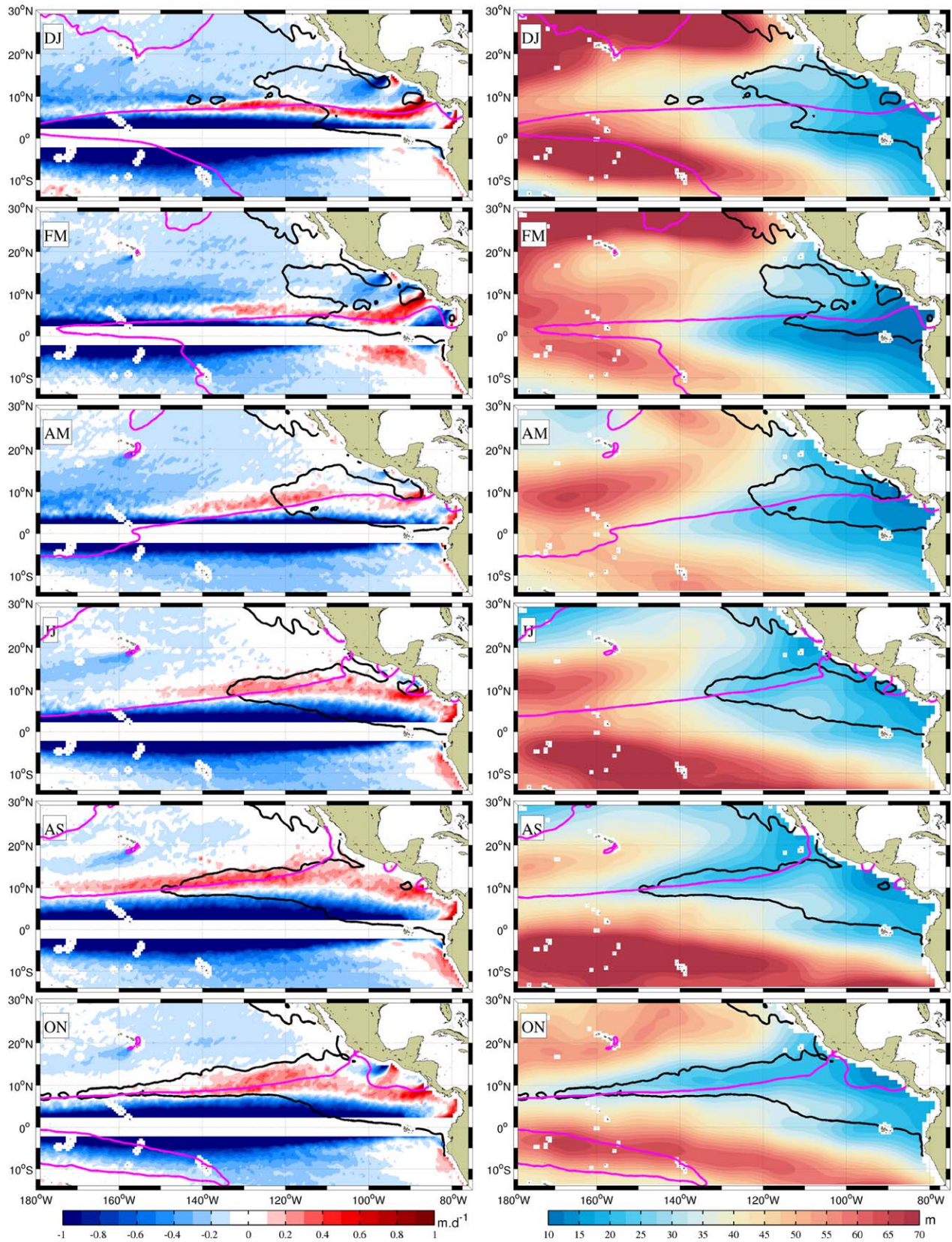


Figure 5. (left) Bimonthly vertical Ekman pumping estimates in m/d derived from ASCAT wind stress and (right) IPRC/APDRC mixed layer depth in meter fields averaged over 2010–2015. The black and magenta thick contours are the 34 isohaline and location of the ITCZ, respectively. From top to bottom the bimonthly average corresponds to months as shown in Figure 3.

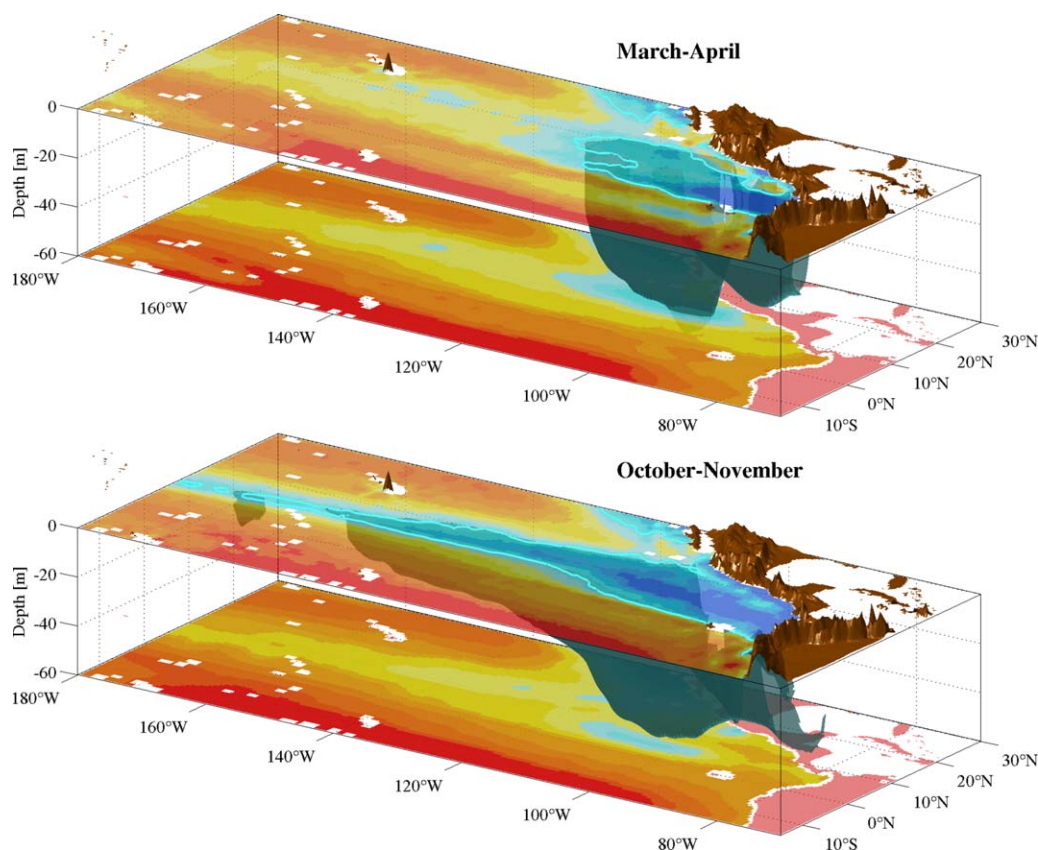


Figure 6. Three-dimensional bimonthly variability of the EPFP averaged over 2010–2015 derived by combining SMOS SSS at the surface and Argo OI analyses at depth (ISAS). The dark blue waters are indicating $S \leq 34$. The cyan blue contours are the surface isohaline at 34. (top) March–April. (bottom) October–November bimonthly averages.

$$V = \iiint_V (\Gamma(34 - S(x, y, z))) dx dy dz \quad (2)$$

where Γ is the Heaviside function ($\Gamma=1$ when $SSS \leq 34$ and 0 otherwise). The domain A corresponds to 180°W – 75°W and 5°S – 20°N . The northern boundary of the domain is set to 20°N , because northward of this latitude, freshwater below 34 associated with the California current can occur. The volume V is evaluated over domain A down to 110 m depth.

EPFP surface area estimated from SMOS SSS nearly doubles from $\sim 4.7 \times 10^6$ km² in April to $\sim 9.5 \times 10^6$ km² in November (Figure 8). EPFP seasonal cycles of area and volume are well correlated, with average EPFP thickness ~ 30 m. SMOS and ISAS EPFP area estimates are consistent to within 10%, with the former slightly larger in May–December. SMOS has higher spatial resolution, denser coverage, and is more near-surface than ISAS, which might explain the difference. West of 150°W , $SSS < 34$ is observed in SMOS in October–November while ISAS does not resolve these very shallow surface lenses (Figure 7).

4. Interannual Variability of the EPFP Over 2010–2015

We analyze hereafter the interannual variability in the salinity signature of the EPFP and of its major forcing fields (E-P, currents, and wind stress) during the SMOS satellite period (from 2010 to 2015). We also compare it to the one observed from in situ observations collected over the last decade (section 4.1). We focus on SSS and its forcing fields during the April–May and October–November months for these two particular years (section 4.2). We further analyze the EPFP interannual surface and subsurface signatures in the central Tropical Pacific where the most significant variability was found (section 4.3).

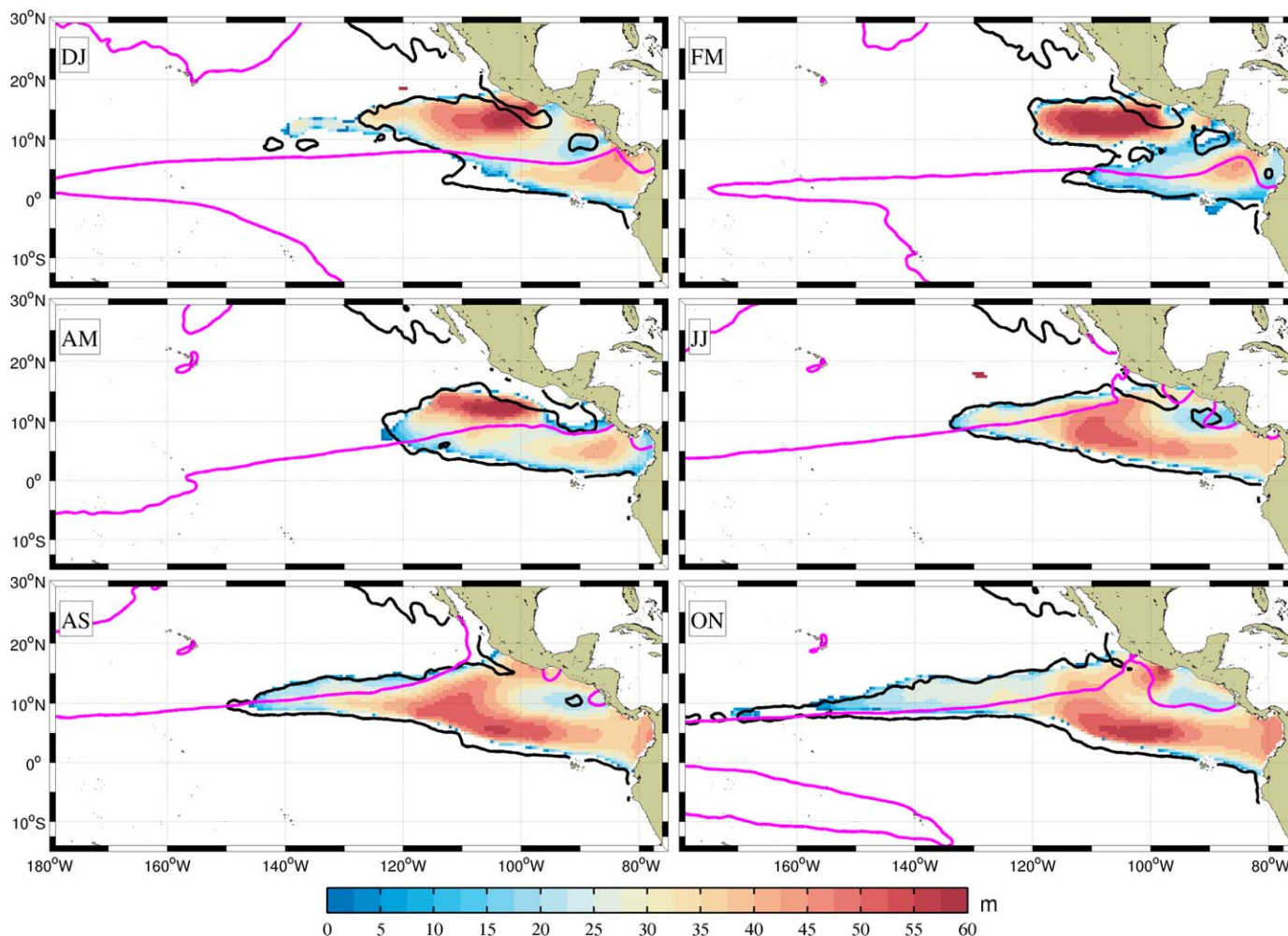


Figure 7. Bimonthly variability of the subsurface 34-isohaline depth (meter) averaged over 2010–2015 and derived from Argo OI monthly analyses (ISAS). The thick black contour is the surface 34-isohaline from SMOS data.

4.1. Interannual Variability of the EPFP Extent

The EPFP surface areas from analyzed data (ISAS) and SMOS both show a strong seasonal cycle with interannual variations (Figure 9). In average, the EPFP area is $\sim 6.5 \times 10^6 \text{ km}^2$ with a seasonal variation of $\sim \pm 2.3 \times 10^6 \text{ km}^2$. The root mean square difference between SMOS and ISAS over the 2010–2015 period is about $5 \times 10^5 \text{ km}^2$, which corresponds to a mean relative difference of 4% and never exceeds 10%.

The interannual variability of the pool can be as high as 2.5 times the seasonal cycle amplitude, as, for example, between 2012 and 2015. Both ISAS in situ products (blue curve) and SMOS (black curve) satellite estimates reveal that a minimum ($\sim 7.14 \times 10^6 \text{ km}^2$) in the maximal extent of the EPFP is reached in 2012. In contrast, 2014–2015 years are characterized by the largest extents of the EPFP area observed during the last 12 years (about 11 and $13 \times 10^6 \text{ km}^2$ in November 2014 and 2015, respectively). These are twice and up to ~ 3 times higher than the 12 year averaged seasonal cycle, respectively.

4.2. 2012 and 2015: Two Extreme Years

SSS, precipitation, wind stress, and surface currents fields in April–May (minimal extent, Figure 10) and October–November (maximal extent, Figure 11) reveal marked differences in between the two extreme years 2012 and 2015.

In April–May, the EPFP that is usually trapped east of 120°W by the NECC and eroded north by the trade winds during winter, is 1.6 times larger in 2015 than in 2012. Remarkably, the western and central part of the tropical Pacific ocean are clearly saltier (around 0.4) in 2012 than in 2015.

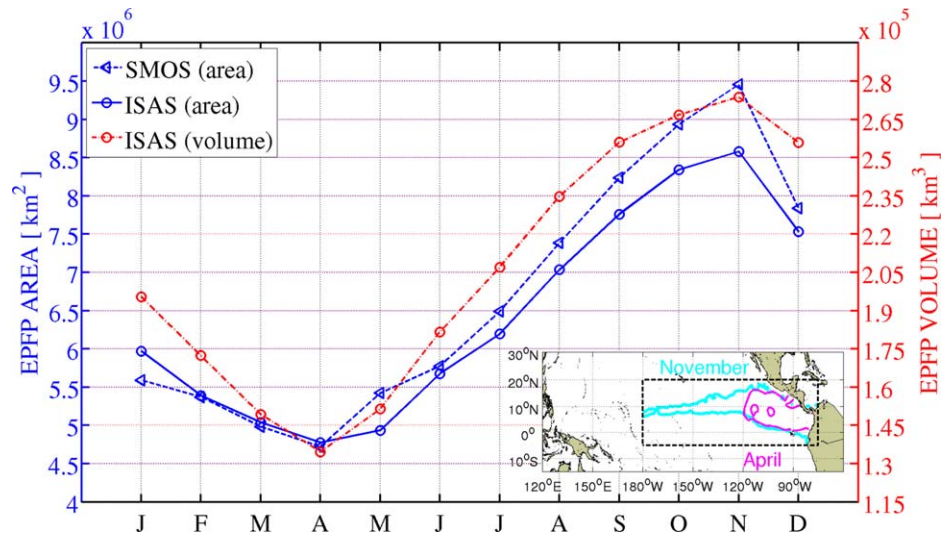


Figure 8. Monthly average fresh pool areal extent over 2010–2015 deduced from ISAS salinity analysis (solid circle blue curve) and SMOS fields (dash triangle blue curve). Monthly average fresh pool volume deduced from ISAS corresponds to the solid red circle dashed curve.

The 28°C isotherm (gray contour in Figure 10, top row) shows that the west Pacific warm pool (WPWP) joins the EPWP in 2015 indicating a strong SST increase of the whole tropical Pacific between 2012 and 2015. The precipitation patterns (Figure 10, second plots) indicate that very low rainfall occurred during spring in the central Pacific in 2012 with respect to spring 2015.

The wind stress patterns are also significantly different between these 2 years with much lower values west of 180°W in 2012 compared to 2015. In the central Pacific (180°W, 150°W; 4°N, 12°N), wind stress τ was in contrast significantly higher in 2012 than in 2015 with the highest values ($>0.08 \text{ N m}^{-2}$) displaced equatorward. The ITCZ found south of the equator in 2012 seems to correspond to the South Pacific Convergent Zone (SPCZ) location. The ITCZ apparently disappeared at that time in the Central Pacific.

According to Stommel’s theory [Stommel, 1948], the meridional distribution of τ is a key driver of the equatorial current system. This is clearly evidenced by the differences in current maps between 2012 and 2015: the NECC is narrower and weaker around the dateline in 2012 and is located slightly more southward (below 4°N) than in 2015.

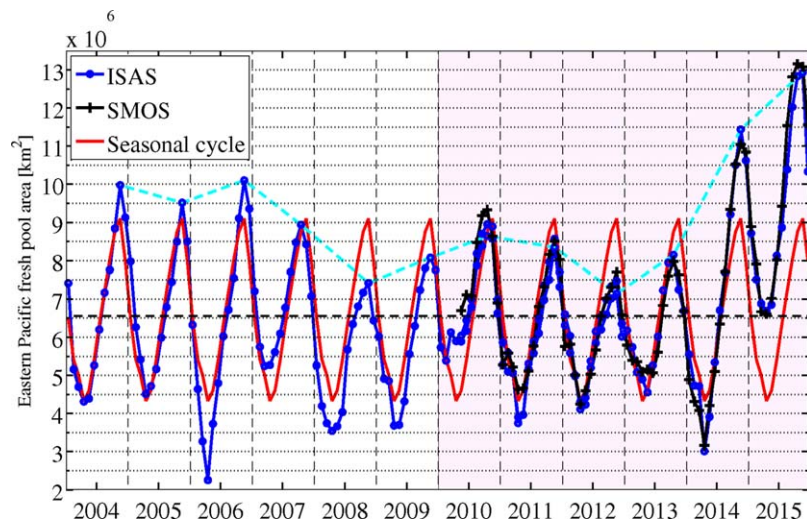


Figure 9. Time evolution of the EPFP area during the 2004–2015 period based on ISAS (blue dotted curve) and the corresponding seasonal cycle over the period (red curve). Estimates based on SMOS data correspond to the black curve. The maximum areal extent of the pool of each year is emphasized by the cyan dashed curve.

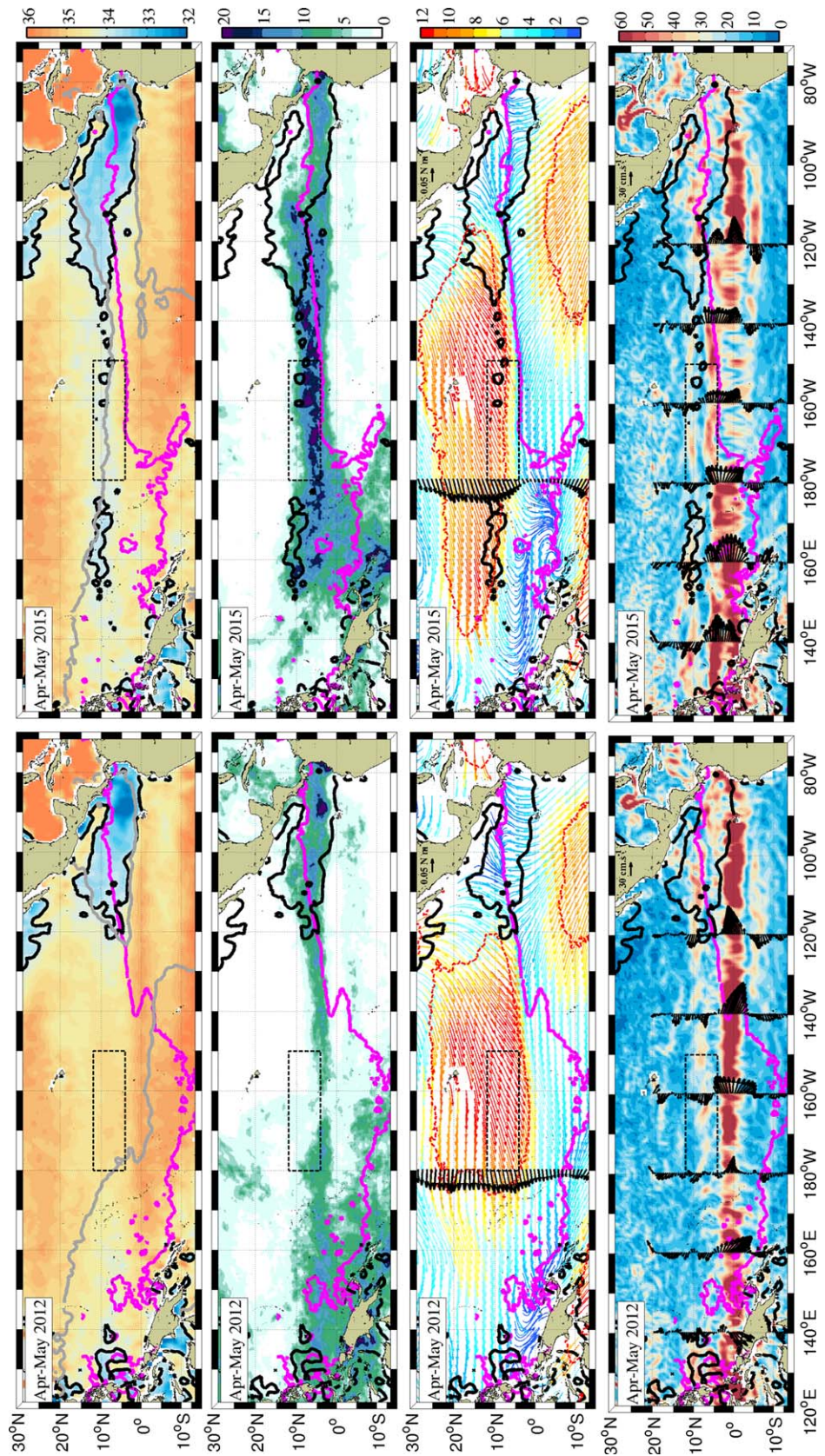


Figure 10.

The SSS fields also exhibit significant differences between 2012 and 2015 for the October–November months (Figure 11). The 34-isohaline of the WFPF and EPFP merge in the central Pacific in 2015 when the EPFP stopped at 145°W in 2012. The EPFP extent in autumn is 75% larger in 2015 than in 2012, with maximum salinity differences found around the Equator between 170°E and 160°W, reaching more than 1.25.

The precipitation maps indicate intense rainfall both in 2012 and 2015 but with strong spatial pattern differences. In fall 2012, rainfalls were well aligned with the ITCZ while in 2015, heavy rainfalls occurred with a more patchy distribution, in particular between 160°E and 160°W.

The major feature of the surface currents maps is the presence of a well-delineated intense NECC in 2015 not clearly seen in 2012. Analyzing Lagrangian drifter data within the Central Pacific (CP) box defined by [180°W, 150°W; 4°N, 12°N], it seems that the NECC was too weak to enable drifters to go east of 150°W in 2012 (Figure 12a). Contrarily, in 2015 and south of 8°N, almost all drifters traveled straightly eastward across the box (Figure 12b). Figure 12d shows the average OSCAR currents latitudinal profile at the same longitude and illustrates that the NECC was particularly weak in 2012 with a local maximum of 20 cm/s at 5.5°N, compared to 70 cm/s in 2015. Actually, the NECC is shifted southward in 2012 by about 3° compared to the 2015 situation with a maximum around 1°N–2°N.

The zonal wind stress latitudinal profile (Figure 12c) averaged around 165°W \pm 5° and over the May–October period indicates stronger values in 2012 than the 2004–2015 climatology by 30%. The situation in 2015 is characterized by very low wind stress values compared to the 2004–2015 climatology and even small positive values (eastward direction) around 6°N.

4.3 Interannual Variability in the Central Pacific

4.3.1. Variability at the Surface and in the Atmosphere

The CP box [180°W, 150°W; 4°N, 12°N] is a key area to describe the zonal dynamics of the EPFP. Thirty percent of its total extent is localized here between September and November in average during the 2010–2015 period. A large interannual variability of the EPFP extent is also observed in this domain (20% in 2012, 40% in 2014 and 50% in 2015). In the following, the interannual variability of the key parameters affecting the EPFP dynamics within that region is analyzed.

First, Figure 13 reveals that in 2012, the accumulated rain in this area was 24% lower than the derived 2004–2015 climatology whereas, in 2014 and 2015, it was >20% greater. The difference is even greater if we consider only the 6 first month of the year: the accumulated rainfall is 43% lower in 2012 whereas, in 2014 and 2015, it was 30% and 54% greater, respectively.

Second, the seasonal cycle (monthly median values) of the SSS, SST, zonal current and zonal wind stress in the CP box for three different years: 2012, 2014, and 2015 is compared to the 2004–2015 averaged seasonal cycle (Figure 14). In average, SSS in the CP box reaches a maximum around May and a minimum in November with a \sim 0.5 amplitude (Figure 14a). In 2012 and 2015, the seasonal cycle amplitude is rather similar but with an annual mean SSS that is shifted toward a saltier value (+0.2) in 2012 and a fresher value (–0.4) in 2015. In 2014, the median SSS values in the CP box drop from 34.75 in April to 33.92 in November corresponding to a 0.8 amplitude.

The median SST in the CP box (Figure 14b) exhibits a maximum around September and a minimum around February. The SST during 2012 was 0.3 cooler than the 2004–2015 average, whereas SST in 2014 was 0.35 warmer. The SST values in 2015 are exceptionally high, peaking in September at 29.8°C.

The zonal surface current showed in Figure 14c also indicates that in average over the last 12 years, the currents are dominantly flowing westward during the first half of the year (negative values) and eastward during the second half of the year. The westward zonal current was slightly larger in 2012, followed by a weaker reversal occurring one month later than in the average conditions. The situation in 2014 and 2015 was clearly different with almost no westward flow at the beginning of the year and a particularly intense eastward current (NECC) during the second half.

Figure 10. (top row) SMOS SSS, (second row) CMORPH precipitation in mm/d, (third row) Ascet wind stress in 10^{-2} N m $^{-2}$, and (bottom row) OSCAR surface currents in cm/s maps averaged from April to May for the year (left) 2012 and (right) 2015. The black and magenta contours show the 34 isohaline and ITCZ locations, respectively. The grey contour in top row figures correspond to the 28 isothermal and the dashed black lines indicate the Central Pacific box (CP box) defined by [180°W, 150°W; 4°N, 12°N]. In the third row, the dashed red contours correspond to the locations where $\tau = 0.08$ N m $^{-2} \approx 7$ m/s.

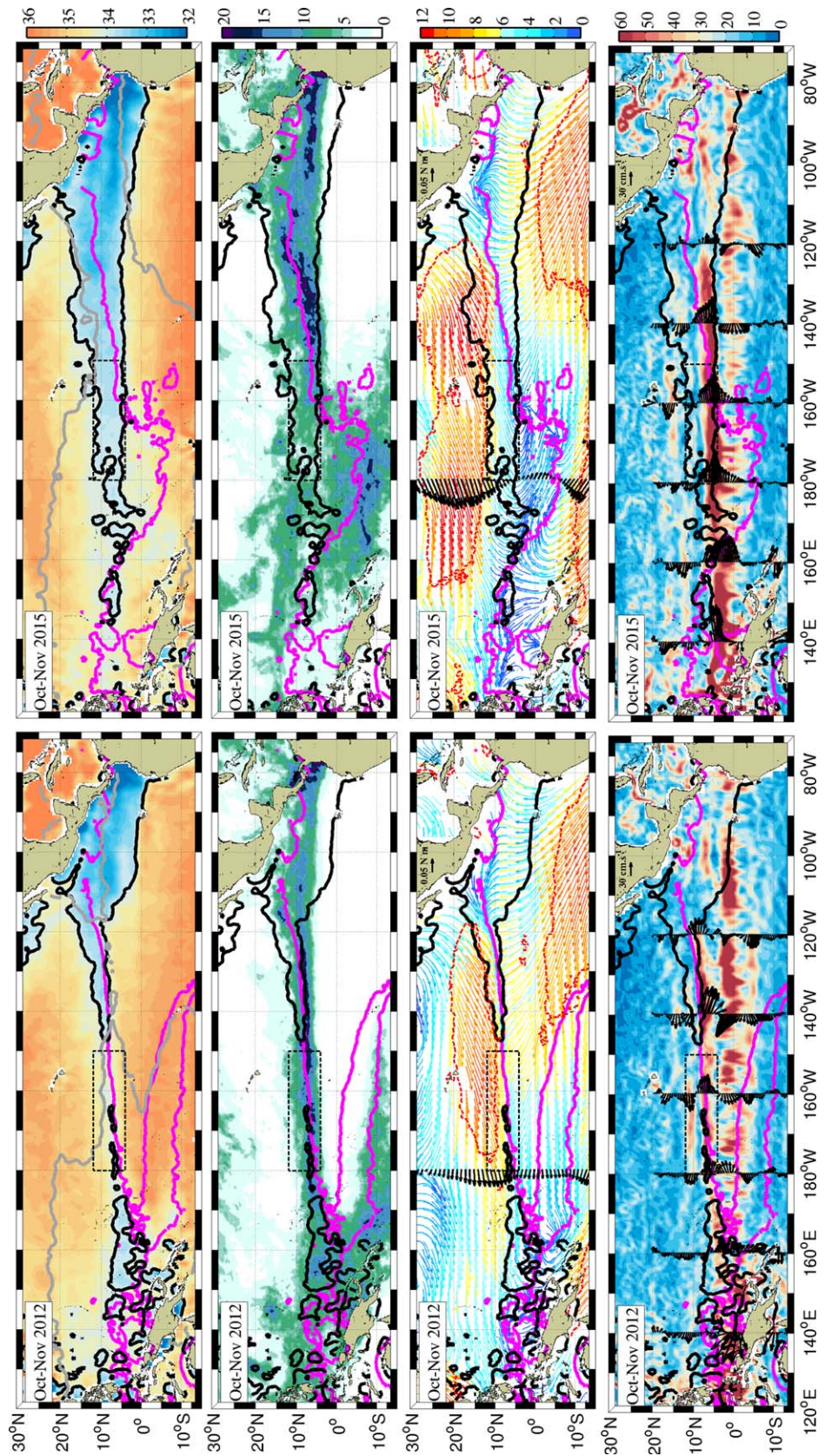


Figure 11.

The zonal wind stress component (negative westward), presented in Figure 14d, is in average maximum ($\sim 0.11 \text{ N m}^{-2}$) around March–April. It decreases slowly by a factor of two ($\sim 0.05 \text{ N m}^{-2}$) until September–October and increases rapidly in December. The zonal wind stress in 2012 was larger than the 2004–2015 average whereas 2014 and 2015 exhibit lower monthly median values. In 2015, the zonal wind stress was almost null in average in the CP box between July and October.

The previous analyses illustrated the significant interannual variability of the SSS and its major surface forcing fields in the central Pacific between 2012 and 2015. Year 2014 was also considered to look for forerunner signatures of the extreme EPFP extent of 2015. Results revealed that:

1. The minimum EPFP extension year 2012 was characterized by higher SSS (+0.2), colder SST (-0.3°C) all year long and slightly stronger westward zonal current and wind stress (+10–25%) during the first half of the year compared to the ones observed in average over the last 10 years.
2. The maximum EPFP extension year 2015 was characterized in the CP box by significantly lower SSS (-0.4), warmer SST ($+0.5 \pm 1^\circ\text{C}$), zonal currents that were only flowing eastward all year long and significantly lower wind stresses particularly during the second half of the year compared to the ones observed in average over the last 10 years.
3. During year 2014 in the CP box, SSS exhibited a significantly stronger seasonal decrease in SSS (-0.8) than in average (-0.5), leading to a much fresher SSS at the beginning of 2015 than usually.

4.3.2. SubSurface Variability in the CP Box

We further investigate how these interannual changes at the air-sea interface relate to the upper ocean vertical structure in the CP box. The Mixed Layer Depth (MLD) and the top of the thermocline are both observed to progressively shoal from an average depth of $\sim 60 \text{ m}$ before 2012 to $\sim 40 \text{ m}$ reached in 2015. The excess precipitation (Figure 15b) and the decrease in wind stress intensity (Figure 15a) in 2014–2015 with respect to 2012 both contribute to a significant freshening of the mixed layer and its shoaling. Upper ocean warming and freshening in 2014–2015 likely resulted in a more buoyant surface layer. This decrease of surface density, concomitant with a decrease in wind stress intensity both combine to limit the upper ocean mixing during winter 2014–2015. Changes in the Brunt-Väisälä frequency and its vertical distribution, $N^2(z)$, partly illustrate these processes (Figure 15e). The depth where $N^2(z)$ reaches a maximum value (N_{max}^2) is also provided. The stratification in between the MLD and 100 m depth is seen to significantly increase from an average value of $\sim 20\text{--}25 \text{ cph}$ during 2010–2013 to about $30\text{--}35 \text{ cph}$ in 2014 and 2015. This increase in stratification is associated with a steep shoaling of N_{max}^2 from an almost constant depth of 110 m from 2010 to mid-2014 to about 50 m depth later on. The relative contribution of salinity and temperature changes to the upper ocean stratification can be evaluated further using $N_S^2 = -g\beta\partial S/\partial z$ and $N_T^2 = g\alpha\partial T/\partial z$, where β and α are the saline contraction and thermal expansion coefficients, respectively. The depths where $N_{S_{\text{max}}}^2 = \max(N_S^2(z))$ and $N_{T_{\text{max}}}^2 = \max(N_T^2(z))$ were also estimated.

As illustrated by Figure 15f, salinity contributes little to the vertical stratification in general, except between 20 and 60 m during the rainy seasons when salinity contributes by $\sim 30\%$ to the total N^2 estimate (consistent with Maes and O’Kane [2014], Figure 5). During the rainy season 2014, salinity contributes by more than 40% to the stratification over the mixed layer.

While the depth of N_{max}^2 exhibits low seasonal variability (Figure 15e), the depth where N_S^2 is maximum shows a very strong seasonal amplitude (Figure 15f), shoaling from 130 m during Spring to 40 m during Autumn. From mid-2014 to end 2015, this seasonal cycle of the vertical migration in the maximum of N_S^2 is almost suppressed. As illustrated in Figure 15e, the shoaling of N_{max}^2 (white curve) during the end of 2014 and beginning of 2015 is mostly due to the shoaling of $N_{S_{\text{max}}}^2$; the depth $N_{T_{\text{max}}}^2$ (cyan curve) is observed to shoal latter during summer 2015.

5. Summary and Discussions

The eastern Pacific fresh pool (EPFP) variability during the SMOS SSS satellite period has been analyzed combining SSS fields with complementary oceanic and atmospheric data. In particular, this work aimed at

Figure 11. (top row) SMOS SSS, (second row) CMORPH precipitation in mm/d, (third row) Ascet wind stress in 10^{-2} N m^{-2} , and (bottom row) OSCAR surface currents in cm/s maps averaged from October to November for the year (left) 2012 and (right) 2015. The black and magenta contours show the 34 isohaline and ITCZ locations, respectively. The grey contour in top row figures corresponds to the 28 isothermal. In the third row, the dashed red contours correspond to the locations where $\tau = 0.08 \text{ N m}^{-2}$.

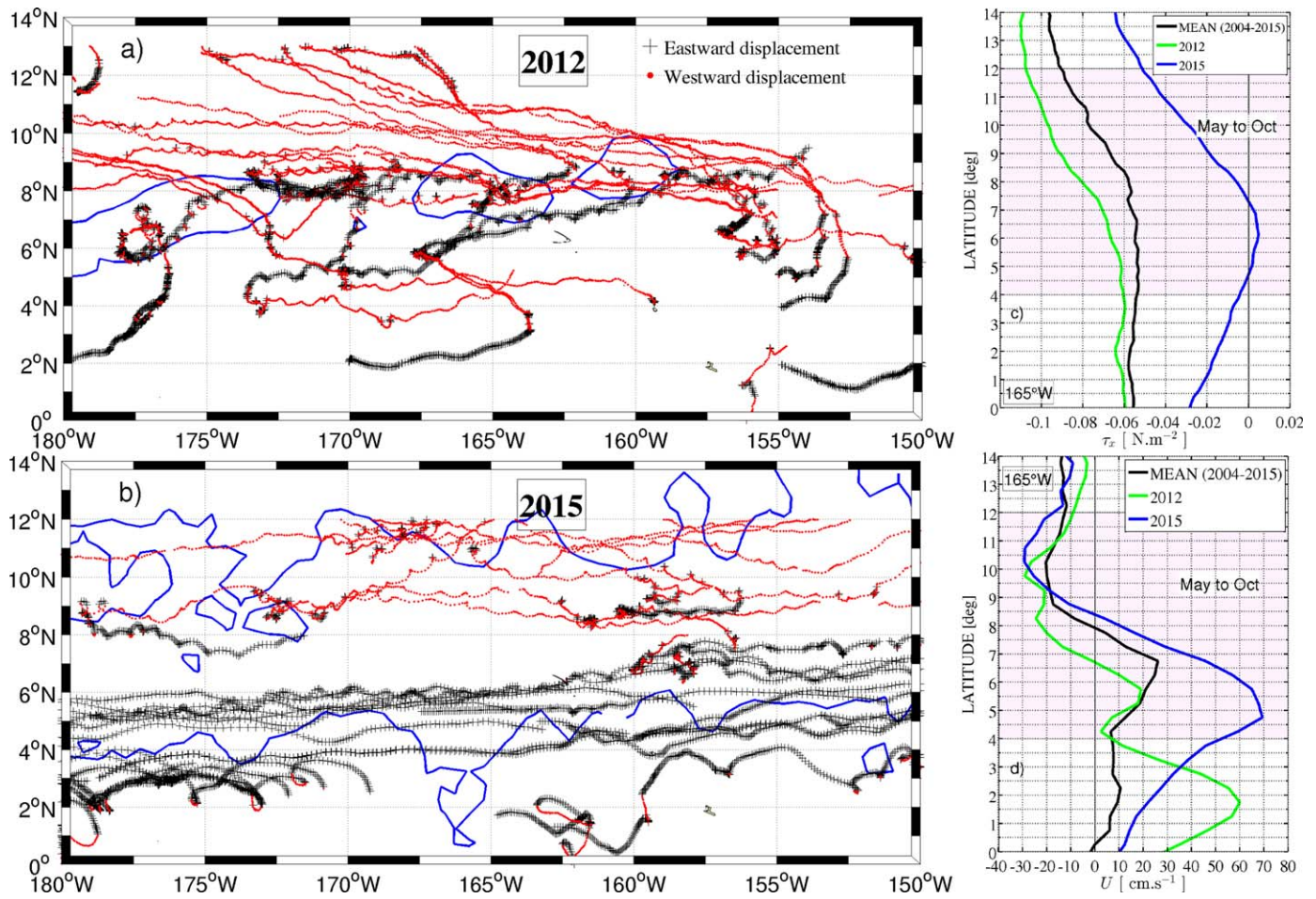


Figure 12. From May to October, all available drifters are shown in Figures 12a and 12b for the year 2012 and 2015, respectively. The black plus symbols indicate drifters' position with positive zonal velocity (eastward displacement) and red dots, negative zonal velocity (westward displacement). The blue contour in Figure 12b shows the maximal extent of the EPFP occurring in November 2015. Figures 12c and 12d show latitudinal profiles of zonal wind stress and OSCAR zonal currents average from May to October and in the longitudinal band $165^{\circ}W \pm 5^{\circ}$.

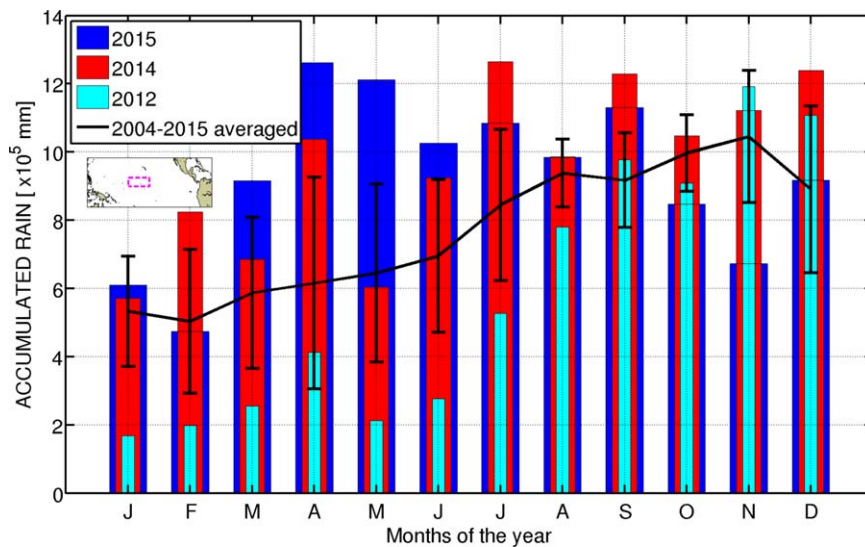


Figure 13. Monthly rain fall accumulation in 2012 (cyan bars), 2014 (red bars), and 2015 (blue bars) in the CP box (Figure 10, dashed box). The black solid line is the monthly rain fall accumulation climatology based on the 2004–2015 period with error bars corresponding to one standard deviation for each calendar month.

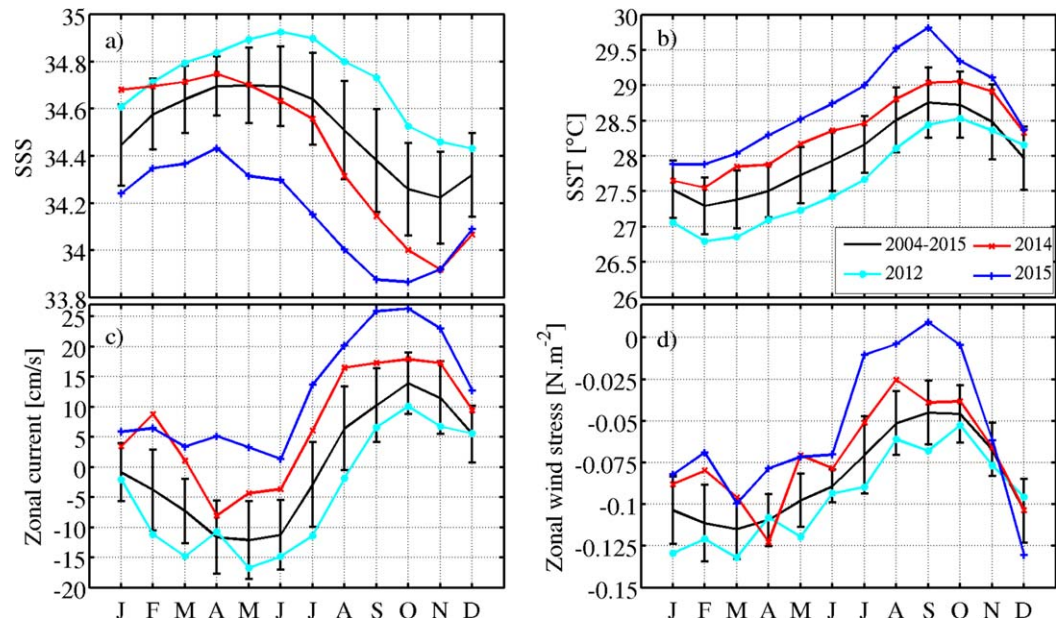


Figure 14. (a) SSS, (b) SST, (c) zonal current, and (d) zonal wind stress monthly median values in the CP box (Figure 10, dashed box) for the year 2012 (cyan curves), 2014 (red curves), 2015 (blue curves), and the 2004–2015 period (black curves). The error bars corresponding to one standard deviation of the 12 January months, February months, etc.

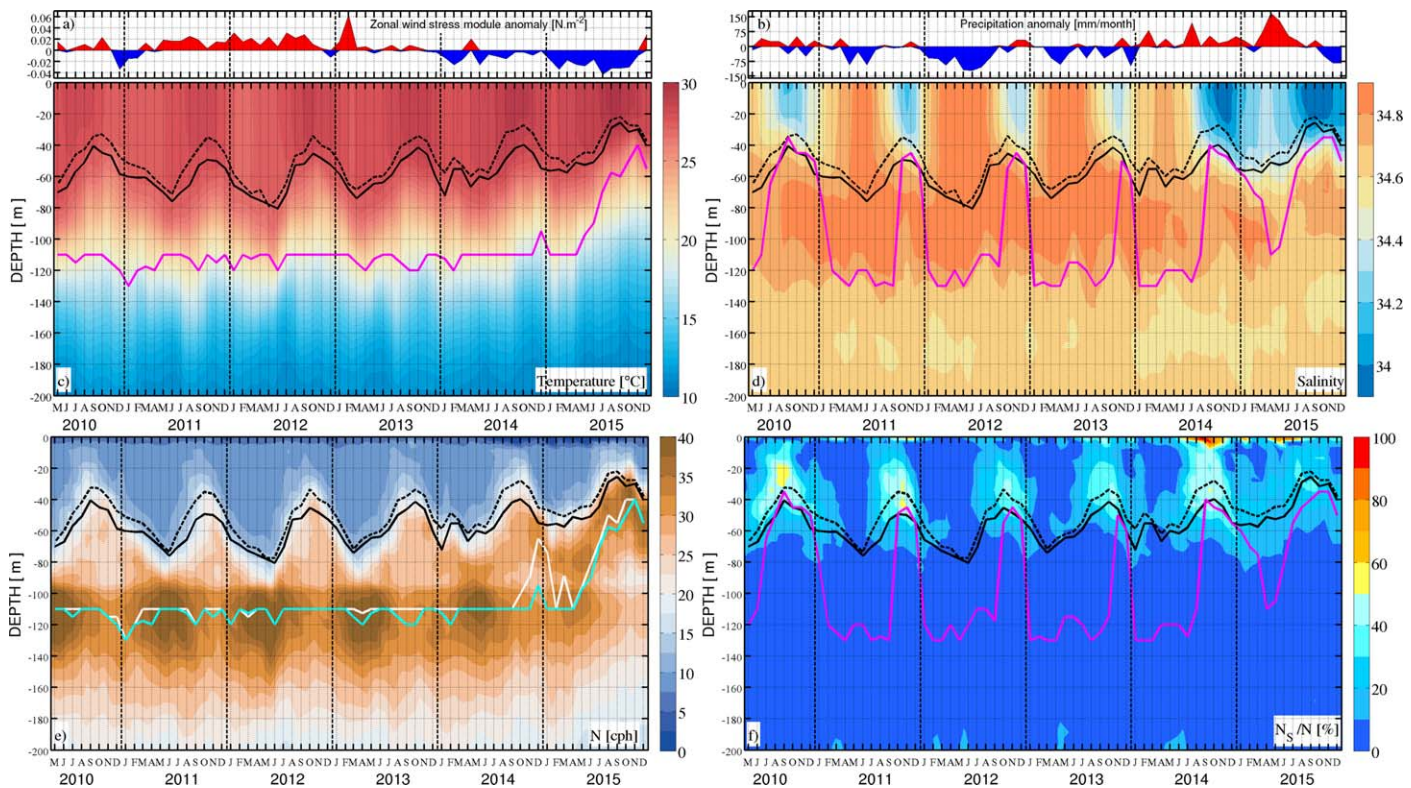


Figure 15. From May 2010 to December 2015, zonal wind stress module anomaly and precipitation anomaly averaged in the CP box (Figure 10, dashed box) are shown in Figures 15a and 15b (top plots). Time-Depth diagrams of temperature, salinity, Brunt-Väisälä frequency (N^2) and percentage of the salinity contribution to the stratification frequency (N_s/N^2), averaged in the CP box, correspond to Figures 15c–15f, respectively. The dashed and solid black curves indicate the depth of the mixed layer (MLD and the top of the thermocline (TTD), respectively. The magenta lines indicate the depth where N^2 is maximum in Figure 15c and the depth where N_s is maximum in Figures 15d and 15f. In Figure 15e, the white and cyan curves indicate the depth where N^2 and N_s is maximum, respectively.

describing the seasonal and interannual zonal displacements of the EPFP and the links between the pool surface and subsurface processes. The fresh pool is defined by tropical surface water (TSW) with $SSS \leq 34$ [Wyrtki, 1966]. We take advantage of 5 years of satellite SSS observations from SMOS mission to extend previous observational study, which mostly focused on the far eastern part defined by tropical surface waters with $SSS \leq 33$ [Alory *et al.*, 2012], or, on the meridional dynamics of the low SSS minimum zone [Yu, 2014, 2015].

The EPFP and associated TSW variability are found closely related to changes in freshwater fluxes, wind stress, and surface currents at seasonal time scales. The seasonal cycle of the EPFP's surface area reveals two phases:

1. An extension phase: the EPFP reaches its minimum extent ($4.3 \times 10^6 \text{ km}^2$) in April following the dry season (January–April). At that time, the pool extends from equator to 15°N and is observed only east of 125°W . The EPFP is found in general thicker on its northern flank ($>40 \text{ m}$, north of $\sim 10^\circ\text{N}$) than on its southern flank ($<25 \text{ m}$). The western tip of the pool is located in April at $\sim 12.5^\circ\text{N}$ where the North Equatorial Counter Current (NECC) is found maximum. From April to September, there is a continuous stretching of the pool westward to reach $\sim 170^\circ\text{W}$. Remarkably, the westward extension of the pool toward central Pacific occurs in a latitudinal band (4°N – 12°N) dominated by the eastward flowing NECC. Only the northern flank of the pool is under the influence of the weaker westward flowing North Equatorial Current (NEC). Therefore, the westward extent of the EPFP is mostly induced by heavy rainfalls under the ITCZ and westward freshwater advection by the NEC.
2. A contraction phase: In November, the EPFP's extent is maximum ($9 \times 10^6 \text{ km}^2$) and reaches central Pacific (150°W – 180°W). In this region, the pool is rather shallow with a thickness on the order of 10–20 m. Satellite SSS (at a spatial resolution of $0.5^\circ \times 0.5^\circ$), which is an interfacial measurement of upper ocean salinity (within the first centimeters below the surface) reveals a slightly greater pool area (greater up to 10%) than the one deduced from the low spatial resolution ($\sim 3^\circ \times 3^\circ$), 1–5 m depth objectively analyzed in situ data. The differences are particularly evident during the rainy season. The pool area then decreases rapidly until January due to the southward displacement of the ITCZ, letting behind the shallow part of the EPFP in the central Pacific. The fresh surface water accumulated in this zone is then rapidly eroded by the increasing trade winds which induce vertical mixing with saltier water from below, and northward Ekman transport.

The interannual variability of the EPFP has been further analyzed over the relatively short SMOS SSS observation period (5.5 years) and compared to the one derived from the last 12 years of in situ observations (Figure 9). As revealed, the interannual variability of the pool areal extent can be twice as important as the amplitude of its seasonal variability. Interestingly, during the satellite period, two extrema in the maximum seasonal extension of the pool have been observed. At the end of the 2012s rainy season, the latter was $7.5 \times 10^6 \text{ km}^2$, well below the last 12 year averaged value ($9 \times 10^6 \text{ km}^2$). Contrastingly, in 2015, the pool maximal extension reached an extreme value of $13 \times 10^6 \text{ km}^2$, coinciding with the occurrence of a strong El Niño event.

The spatial distributions of SSS during spring and autumn have been compared with the ones of the accumulated rainfalls, wind stresses, and surface currents for those two extreme years (Figures 10 and 11). The different phases of the El Niño-Southern-Oscillation (ENSO) are clearly evidenced by the changing patterns in the previous fields, most evident in the central Pacific. The year 2012 (corresponding to a La Niña phase) is characterized by negative precipitation anomalies in the central Pacific linked to a southward shift of the ITCZ and positive trade wind anomalies during the first half of the year. Contrastingly, above normal precipitation occurred during the dry seasons of 2014 and 2015, accompanied by weaker trade winds. The differences in the wind stress patterns between 2012 and 2014–2015 induced a clear change in the equatorial currents, particularly affecting the intensity of the NECC in the region of the EPFP maximal zonal extension (180°W – 150°W ; 4°N , 12°N).

In this central Pacific region (CP box), the 12 year average seasonal cycle reveals that SSS is generally maximum around May and minimum in November with a ~ 0.5 amplitude. In 2012 and 2015, the seasonal cycle amplitude is comparable, but with an annual mean SSS that is saltier (+0.2) in 2012, and significantly fresher (−0.4) in 2015. In 2014, the amplitude of the SSS seasonal cycle is significantly increased, reaching 0.8, mostly due to a steep freshening occurring during the rainy season. In the CP box, precipitations are seasonally minimum in January and maximum in November. A deficit in accumulated rainfall of 43% in

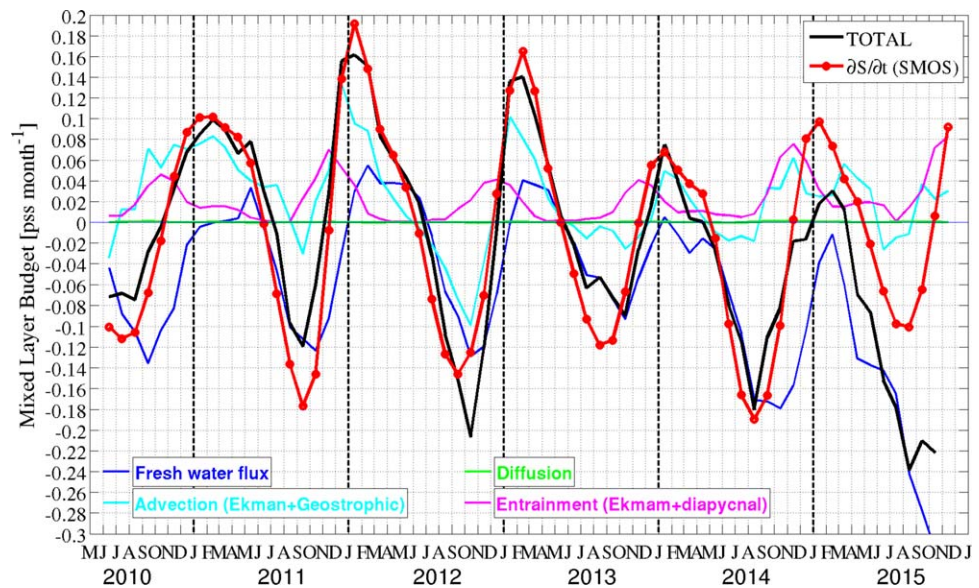


Figure 16. From May 2010 to December 2015, monthly averaged terms of the slab mixed-layer salinity budget model of equation (3) evaluated over the CP Box (Figure 10, dashed box). The blue, cyan, pink, and green curves are showing the freshwater flux (FWF), the horizontal advection ($-\mathbf{u} \cdot \nabla S$), the vertical Ekman entrainment and diffusion terms ($-\kappa \nabla^2 S$), respectively. The black curve is the sum of all model terms and the red is showing the SSS trend $\partial S / \partial t$ derived from SMOS.

2012 and an excess of 30% and 54%, in 2014 and 2015, respectively, are observed during the first 6 months of these years.

During the second half of the year, precipitations for all years are comparable to the 12 year average values. The large precipitation excesses during the dry season 2014 explain the large salinity drop observed in winter of the same year. Added to another above normal accumulated rainfall during the follow-on dry season 2015, both preconditions potentially triggered an abnormal fresh pool extent observed in November 2015. The surface currents in the CP box dominantly flow westward during the first 6 months to reverse eastward the rest of the year. The seasonal cycle of the zonal currents in the CP box is different in 2014 and 2015 compared to 2012, exhibiting only eastward component throughout these two years, as clearly illustrated by surface drifters trajectories (Figure 12). Over the last 12 years, the zonal wind stress intensity averaged over the CP box is maximum around march and minimum in September–October. In 2012, the latter was slightly higher than the 12 year average whereas, in 2014 and 2015, it was clearly lower all year long, particularly from June to October 2015.

The excess precipitation and the decrease in wind stress intensity in 2014–2015 with respect to 2012 both contributed to a significant freshening of the mixed layer and its shoaling (by ~ 20 m). These two effects combined to increase the buoyancy of surface waters, and the relative contribution of salt to the strength of vertical stratification. Upper ocean mixing during winter 2014–2015 was probably inhibited by a significant increase of stratification at the base of the mixed layer. These effects might have favored an extreme extent of the EPFP area in 2015.

To gain further insights into the analysis of the dominant physical mechanisms involved in the observed seasonal and interannual SSS variability, a mixed-layer salinity budget within the CP box is finally conducted hereafter. Consider a mixed-layer model where the salinity S , and the horizontal current \mathbf{u} are constant within a mixed layer of depth h . The vertically integrated salinity equations can be written

$$\frac{\partial S}{\partial t} = \underbrace{\frac{S(E-P)}{h}}_{\text{FWF}} + \underbrace{\frac{S-S_d}{h} \Gamma(w_e) w_e}_{\text{Entrainment}} - \underbrace{\mathbf{u} \cdot \nabla S}_{\text{Advection}} - \underbrace{\kappa \nabla^2 S}_{\text{Diffusion}} \quad (3)$$

where Γ is the heaviside function, w_e the entrainment velocity, E the evaporation, and P the precipitation rate. Following Michel *et al.* [2007], the horizontal mixing coefficient κ is chosen equal to 2000 m s^{-2} . If the mixed layer is deepening, there is entrainment of water from below the mixed layer (denoted by the minus

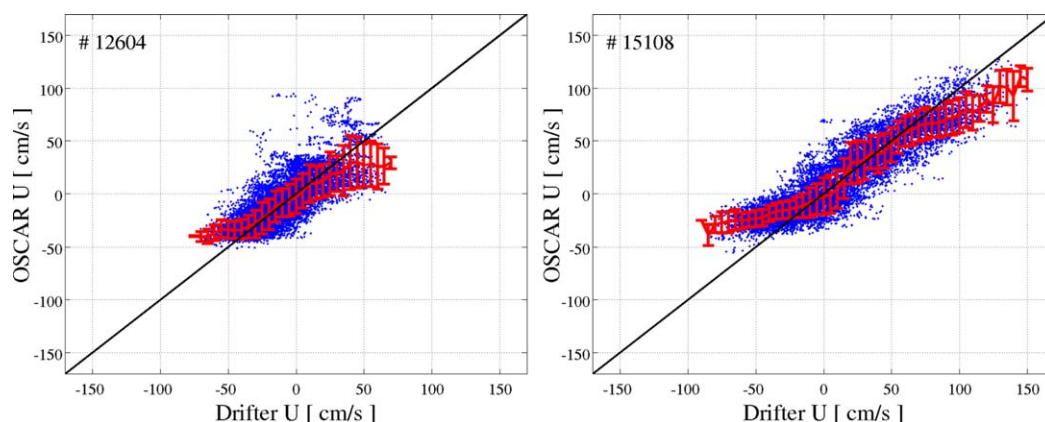


Figure 17. Scatter plot of zonal current components estimate from drifters compared to OSCAR currents field (5 days, third degree) value interpolated at each drifter time and location. Left and right figures correspond to all the available drifter measurements in the CP box (Figure 10, dashed box) in 2012 and 2015, respectively.

index), whereas if it is shoaling, there is detrainment and fluid is left behind without changing the salinity. S_d correspond to the salinity at the mixed layer depth h .

In general, this simple 1-D mixed layer model is matching rather well the observed SMOS SSS trend with a root mean square difference of 0.04 PSS/month (Figure 16). Nevertheless, from November 2014 onward, we observe the 1-D model to predict a significantly larger freshening than the one deduced from the SMOS satellite observations. Major sources of salinizing in the CP box during the winter season are the horizontal advection of salt by Ekman and geostrophic currents and the vertical Ekman and diapycnal entrainment of saltier water from below the MLD. As revealed in Figure 17, Oscar products systematically underestimate westward (negative) and eastward (positive) currents below 25 cm/s and above 60 cm/s, respectively. These biases might explain an underestimation of the salt advection in our 1-D model. Similarly, there are large uncertainties on the vertical entrainment term by Ekman pumping in an area with very low wind stress in 2014–2015 and very strong eastward current at the base of the Ekman layer [Cronin and Kessler, 2009]. In addition, uncertainties on the E-P fluxes could be also responsible for the observed mixed layer budget discrepancies during the El Niño event.

Nevertheless, an important result of our work illustrated by Figure 16 is the key role of the climatic conditions during the dry seasons (December–April) in preconditioning the zonal extent of the EPFP during the rainy seasons (May–November). In average over 2010–2013, the mixed layer salinity in the CP box increased by ~ 0.6 during the dry seasons. Both the observation and the estimated salt budget reveal that the salinizing was only of ~ 0.2 from December 2013 to May 2014. According to the 1-D model, the weaker salinizing observed during that period was induced by abnormal freshwater fluxes ($E-P \leq 0$) and weaker horizontal advection. Drop in the trade wind intensity and above normal precipitation within the CP box during the rainy season 2014 resulted in fresher salinity within a shallower mixed layer and an enhanced vertical stratification. These processes were likely key conditions that triggered the largest spatial extent of the EPFP during El Niño 2015.

Appendix A: Satellite SSS Validation

SMOS SSS weekly composite products were colocated with Argo floats, ship TSG and Tropical Moorings upper-level salinity measurements. For a given weekly SMOS L4a SSS field, in situ/satellite matchups were

Table 1. Statistics of the Weekly SMOS SSS Products Compared With the Different In Situ Data Sets

	#	MEAN	STD	MEDIAN	IQR	R
TAO	17010	-0.05	0.30	-0.02	0.28	0.90
Argo	28,082	0	0.32	0.01	0.27	0.92
TSG (GOSUD)	56,568	-0.12	0.40	-0.05	0.46	0.90
TSG (SAMOS)	1,049,326	0	0.27	0.01	0.30	0.91

defined by comparing in situ data collected during the week to the SMOS SSS at grid nodes found within a radius of $1/4^\circ$ from the in situ sample. Statistics of the differences between the L4a SMOS SSS and the in situ observations are given in Table 1 for the study area defined by $[5^\circ\text{S}-30^\circ\text{N}, 180^\circ\text{W}-75^\circ\text{W}]$, covering the eastern Pacific fresh pool.

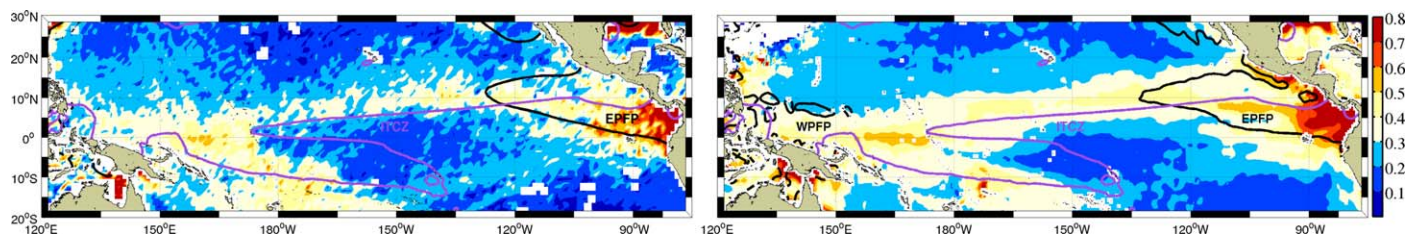


Figure 18. (left) Annual salinity standard deviation from WOA13 at the surface and (right) SMOS in shaded color. Curves in black and purple define the 34-isohaline and meridional wind stress equal to zero, respectively.

Acknowledgments

ESA (living planet fellowship) and IFREMER funded this work. The SMOS L4 data were obtained from the Ocean Salinity Expertise Center (CECOS) of the CNES-IFREMER Centre Aval de Traitement des Données SMOS (CATDS), at IFREMER, Plouzané (France). V01, [May 2010 to December 2015] (<ftp://ext-catds-cecos-ifremer.catds2010@ftp.ifremer.fr/>). This study has been conducted using ISAS products from the Copernicus Marine Service (<http://marine.copernicus.eu>). Surface current products were collected from Ocean Surface Current Analyses Real time (<http://www.oscar.noaa.gov>). We thank the Global Drifter Program (<http://www.aoml.noaa.gov/envids/gld/index.php>) for providing free access to the drifter data. The global ocean evaporation products were provided by the WHOI OaFlux project (<http://oafux.whoi.edu>). Satellite CMORPH rain rate estimates are based on National Center for Atmospheric Research Staff (Eds) data sets (http://www.cpc.ncep.noaa.gov/products/janowiak/cmorph_description.html). Surface wind stress component are based on the Advanced SCATterometer (ASCAT) daily data produced and made available at Ifremer/cersat (<ftp://ftp.ifremer.fr/ifremer/cersat/products/gridded/MWF/L3/ASCAT/>). Monthly Mixed Layer Depth estimates are available at the International Pacific Research Center/Asia-Pacific Data-Research Center (http://apdrc.soest.hawaii.edu:80/dods/public_data/Argo_Products/monthly_mean/Mixed_Layer_Gridded_monthly_mean). Argo floats measurements are provided by the Coriolis data center (<http://www.coriolis.eu.org>). We acknowledge the use of freely available Argo data collected by the International Argo Project and the national programs that contribute to it. We thank the GOSUD Project (<http://www.gosud.org>) and the US Shipboard Automated Meteorological and Oceanographic System (<http://samoss.coaps.fsu.edu/html>) for providing free access to the TSG data.

As evidenced in Table 1, the differences between weekly SMOS L4a SSS and in situ data are generally below 0.1 in the mean, or median, and exhibit a standard deviation on the order of 0.3. As seen in Figure 18, the SSS variability within the zonal band of low-salinity water is in general higher than that uncertainty. In addition, averaging the satellite SSS over monthly time scale shall significantly reduce random errors contributing to the satellite/in situ differences. The correlation coefficients between colocalized satellite and in situ data are systematically high above 0.9. The SMOS L4a SSS are corrected for large-scale biases with ISAS OI fields but the later do not build upon the use of TSG nor TAO data.

References

- Alory, G., C. Maes, T. Delcroix, N. Reul, and S. Illig (2012), Seasonal dynamics of sea surface salinity off Panama: The far Eastern Pacific Fresh Pool, *J. Geophys. Res.*, *117*, C04028, doi:10.1029/2011JC007802.
- Amador, J. A., E. J. Alfaro, O. G. Lizano, and V. O. Magaña (2006), Atmospheric forcing of the eastern tropical Pacific: A review, *Prog. Oceanogr.*, *69*(2–4), 101–142, doi:10.1016/j.pocean.2006.03.007.
- Bentamy, A., and D. C. Fillon (2012), Gridded surface wind fields from Metop/ASCAT measurements, *Int. J. Remote Sens.*, *33*(6), 1729–1754, doi:10.1080/01431161.2011.600348.
- Bjerknes, J. (1969), Atmospheric teleconnections from the equatorial Pacific, *Mon. Weather Rev.*, *97*(3), 163–172, doi:10.1175/1520-0493(1969)097<0163:ATFTEP>2.3.CO;2.
- Bonjean, F., and G. S. E. Lagerloef (2002), Diagnostic model and analysis of the surface currents in the Tropical Pacific Ocean, *J. Phys. Oceanogr.*, *32*(10), 2938–2954, doi:10.1175/1520-0485(2002)032<2938:DMAOT>2.0.CO;2.
- Boutin, J., et al. (2015), Satellite and in situ salinity: Understanding near-surface stratification and sub-footprint variability, *Bull. Am. Meteorol. Soc.*, *89*, 1111–1125, doi:10.1175/bams-d-15-00032.1.
- Boyer, T., and S. Levitus (2002), Harmonic analysis of climatological sea surface salinity, *J. Geophys. Res.*, *107*(C12), 8006, doi:10.1029/2001JC000829.
- Boyer, T., et al. (2015), Changes to calculations of the World Ocean Atlas 2013 for version 2, *Tech. Rep.*, NOAA, Silver Spring, Md.
- Cronin, M. F., and W. S. Kessler (2009), Near-surface shear flow in the Tropical Pacific Cold Tongue Front, *J. Phys. Oceanogr.*, *39*(5), 1200–1215, doi:10.1175/2008jpo4064.1.
- de Boyer Montégut, C., G. Madec, A. S. Fischer, A. Lazar, and D. Ludicone (2004), Mixed layer depth over the global ocean: An examination of profile data and a profile-based climatology, *J. Geophys. Res.*, *109*, C12003, doi:10.1029/2004JC002378.
- de Boyer Montégut, C., J. Mignot, A. Lazar, and S. Cravatte (2007), Control of salinity on the mixed layer depth in the world ocean: 1: General description, *J. Geophys. Res.*, *112*, C06011, doi:10.1029/2006JC003953.
- Donlon, C. J., M. Martin, J. Stark, J. Roberts-Jones, E. Fiedler, and W. Wimmer (2012), The Operational Sea Surface Temperature and Sea Ice Analysis (OSTIA) system, *Remote Sens. Environ.*, *116*, 140–158, doi:10.1016/j.rse.2010.10.017.
- Fiedler, P. C., and L. D. Talley (2006), Hydrography of the eastern tropical Pacific: A review, *Prog. Oceanogr.*, *69*(2–4), 143–180, doi:10.1016/j.pocean.2006.03.008.
- Fiedler, P. C., F. P. Chavez, D. W. Behringer, and S. B. Reilly (1992), Physical and biological effects of Los Niños in the eastern tropical Pacific, 1986–1989, *Deep Sea Res., Part. 1*, *39*(2), 199–219, doi:10.1016/0198-0149(92)90105-3.
- Gaillard, F. (2015), ISAS-13 temperature and salinity gridded fields, SEANO, doi:10.17882/45945.
- Gaillard, F., E. Autret, V. Thierry, P. Galaup, C. Coatanoan, and T. Loubrieu (2009), Quality control of large Argo datasets, *J. Atmos. Oceanic Technol.*, *26*(2), 337–351, doi:10.1175/2008JTECHO552.1.
- Gaillard, F., D. Diverres, S. Jacquin, Y. Gouriou, J. Grelet, M. Le Menn, J. Tassel, and G. Reverdin (2015), Sea surface temperature and salinity from French research vessels, 2001–2013, *Sci. Data*, *2*, 150054, doi:10.1038/sdata.2015.54.
- Gaillard, F., T. Reynaud, V. Thierry, N. Kolodziejczyk, and K. von Schuckmann (2016), In situ-based reanalysis of the global ocean temperature and salinity with ISAS: Variability of the heat content and steric height, *J. Clim.*, *29*(4), 1305–1323, doi:10.1175/jcli-d-15-0028.1.
- Hires, R. I., and R. B. Montgomery (1972), Navifacial temperature and salinity along the track from Samoa to Hawaii, 1957–1965, *J. Mar. Res.*, *30*, 177–200.
- Joyce, R. J., J. E. Janowiak, P. A. Arkin, and P. Xie (2004), CMORPH: A method that produces global precipitation estimates from passive microwave and infrared data at high spatial and temporal resolution, *J. Hydrometeorol.*, *5*(3), 487–503, doi:10.1175/1525-7541(2004)005<0487:camtpg>2.0.CO;2.
- Lumpkin, R., and G. C. Johnson (2013), Global ocean surface velocities from drifters: Mean, variance, El Niño–Southern Oscillation response, and seasonal cycle, *J. Geophys. Res.*, *118*, 2992–3006, doi:10.1002/jgrc.20210.
- Lynn, R. J. (1964), Meridional distribution of temperature–salinity characteristics of Pacific Ocean surface water, *J. Mar. Res.*, *22*(1), 70–82.
- Maes, C., and T. J. O’Kane (2014), Seasonal variations of the upper ocean salinity stratification in the Tropics, *J. Geophys. Res.*, *119*, 1706–1722, doi:10.1002/2013JC009366.
- Maes, C., J. Picaut, and S. Belamari (2002), Salinity barrier layer and onset of El Niño in a Pacific coupled model, *Geophys. Res. Lett.*, *29*(24), 2206, doi:10.1029/2002GL016029.

- Maes, C., J. Picaut, and S. Belamari (2005), Importance of the salinity barrier layer for the Buildup of El Niño, *J. Clim.*, *18*(1), 104–118, doi:10.1175/JCLI-3214.1.
- Michel, S., B. Chapron, J. Tournadre, and N. Reul (2007), Sea surface salinity variability from a simplified mixed layer model of the global ocean, *Ocean Sci. Discuss.*, *4*(1), 41–106, doi:10.5194/osd-4-41-2007.
- Picaut, J., M. Ioualalen, C. Menkes, T. Delcroix, and M. J. McPhaden (1996), Mechanism of the zonal displacements of the Pacific Warm Pool: Implications for ENSO, *Science*, *274*(5292), 1486–1489, doi:10.1126/science.274.5292.1486.
- Reul, N., and Ifremer CATDS-CECOS Team (2015), SMOS Level 4 Thematic SSS Research products—Product User Manual, *Tech. Rep.*, IFREMER.
- Reul, N., J. Tenerelli, and S. Guimbard (2015), SMOS Level 3 & 4 Research products of the Centre d'Expertise Ifremer du CATDS—Algorithm Theoretical Background Document, *Tech. Rep. 1*, IFREMER, Brest, France. [Available at http://www.ifremer.fr/naiad/salinityremotesensing.ifremer.fr/CEC_Products/Documentation/CATDS_CECOS_SMOS_Level4aProducts_ATBD.pdf]
- Risien, C. M., and D. B. Chelton (2008), A global climatology of surface wind and wind stress fields from eight years of QuikSCAT Scatterometer data, *J. Phys. Oceanogr.*, *38*(11), 2379–2413, doi:10.1175/2008jpo3881.1.
- Singh, A., T. Delcroix, and S. Cravatte (2011), Contrasting the flavors of El Niño-Southern Oscillation using sea surface salinity observations, *J. Geophys. Res.*, *116*, C06016, doi:10.1029/2010JC006862.
- Stommel, H. (1948), The westward intensification of wind-driven ocean currents, *Trans. AGU*, *29*(2), 202–206, doi:10.1029/tr029i002p00202.
- Trenberth, K. E., and J. W. Hurrell (1994), Decadal atmosphere-ocean variations in the Pacific, *Clim. Dyn.*, *9*(6), 303–319, doi:10.1007/bf00204745.
- Trenberth, K. E., and J. M. Caron (2000), The Southern Oscillation Revisited: Sea level pressures, surface temperatures, and precipitation, *J. Clim.*, *13*(24), 4358–4365, doi:10.1175/1520-0442(2000)013<4358:TSORSL>2.0.CO;2.
- Wang, X., G. Han, W. Li, X. Wu, and X. Zhang (2013), Salinity drift of global Argo profiles and recent halosteric sea level variation, *Global Planet. Change*, *108*, 42–55, doi:10.1016/j.gloplacha.2013.06.005.
- Wyrtki, K. (1966), Oceanography of the eastern equatorial Pacific Ocean, *Oceanogr. Mar. Biol. Ann. Rev.*, *4*, 33–68.
- Wyrtki, K., and R. Kendall (1967), Transports of the Pacific equatorial countercurrent, *J. Geophys. Res.*, *72*(8), 2073–2076, doi:10.1029/JZ072i008p02073.
- Xie, P., and P. A. Arkin (1995), An intercomparison of gauge observations and satellite estimates of monthly precipitation, *J. Appl. Meteorol.*, *34*(5), 1143–1160, doi:10.1175/1520-0450(1995)034<1143:AIOGOA>2.0.CO;2.
- Xie, S.-P. (1994), Oceanic response to the wind forcing associated with the Intertropical Convergence Zone in the northern hemisphere, *J. Geophys. Res.*, *99*(C10), 20,393–20,402, doi:10.1029/94JC01653.
- Yu, L. (2007), Global variations in oceanic evaporation (1958–2005): The role of the changing wind speed, *J. Clim.*, *20*(21), 5376–5390, doi:10.1175/2007jcli1714.1.
- Yu, L. (2014), Coherent evidence from aquarius and argo for the existence of a shallow low-salinity convergence zone beneath the Pacific ITCZ, *J. Geophys. Res.*, *119*, 7625–7644, doi:10.1002/2014JC010030.
- Yu, L. (2015), Sea-surface salinity fronts and associated salinity minimum zones in the Tropical Ocean, *J. Geophys. Res.*, *120*, 4205–4225, doi:10.1002/2015JC010790.
- Yu, L., and R. A. Weller (2007), Objectively analyzed air-sea heat fluxes for the global ice-free oceans (1981–2005), *Bull. Am. Meteorol. Soc.*, *88*(4), 527–539, doi:10.1175/bams-88-4-527.
- Zhang, R.-H., A. J. Busalacchi, X. Wang, J. Ballabrera-Poy, R. G. Murtugudde, E. C. Hackert, and D. Chen (2009), Role of ocean biology-induced climate feedback in the modulation of El Niño-Southern Oscillation, *Geophys. Res. Lett.*, *36*, L03608, doi:10.1029/2008GL036568.
- Zhu, J., B. Huang, R.-H. Zhang, Z.-Z. Hu, A. Kumar, M. A. Balmaseda, L. Marx, and J. L. Kinter III (2014), Salinity anomaly as a trigger for ENSO events, *Sci. Rep.*, *4*, 6821, doi:10.1038/srep06821.